A Deeper Analysis of Center-Finding Techniques for Tropical Cyclones in Mesoscale Models. Part I: Low-Wavenumber Analysis

DAVID R. RYGLICKI

National Research Council, Monterey, California

DANIEL HODYSS

Naval Research Laboratory, Monterey, California

(Manuscript received 7 May 2015, in final form 5 November 2015)

ABSTRACT

A deeper analysis of possible errors and inconsistencies in the analysis of vortex asymmetries owing to the placement of centers of tropical cyclones (TCs) in mesoscale models is presented. Previous works have established that components of the 2D and 3D structure of these TCs—primarily radial wind and vertical tilt—can vary greatly depending on how the center of a model TC is defined. This work will seek to expand the previous research on this topic, but only for the 2D structure. To be specific, this work will present how low-wavenumber azimuthal Fourier analyses can vary with center displacement using idealized, parametric TC-like vortices. It is shown that the errors associated with aliasing the mean are sensitive primarily to the difference between the peak of vorticity inside the radius of maximum winds and the average vorticity inside the core. Tangential wind and vorticity aliasing occur primarily in the core; radial wind aliasing spans the whole of the vortex. It is also shown that, when adding low-wavenumber asymmetries, the aliasing is dependent on the placement of the center relative to the location of the asymmetries on the vortex. It is also shown that the primary concern for 2D analysis when calculating the center of a TC is correctly resolving azimuthal wavenumber 0 tangential wind, because errors here will alias onto all higher wavenumbers, the specific structures of which are dependent on the structure of the mean vortex itself.

1. Introduction

Historically, when diagnostic analyses of tropical cyclones (TC) are performed, whether from observations or from model simulations, there are a few standard metrics that are usually presented to provide information on the systems. Some basic metrics include minimum sea level pressure, maximum 10-m wind speed, radius of maximum winds (RMW), and radius of gale-force winds. More advanced metrics include accumulated cyclone energy (ACE), integrated kinetic energy (IKE) and destructive potential (Powell and Reinhold 2007), and TC phase (Hart 2003). These metrics are system scale. Some of these metrics, such as the surface pressure minimum and maximum 10-m wind speed, can be calculated in a rather straightforward manner regardless of data source without any additional data processing. ACE and IKE are dependent on conversion of the Cartesian wind components to cylindrical wind components—specifically, to tangential wind. The TC phase requires the values of winds, temperatures, and mass field parameters in a 500-km circle surrounding whatever point is chosen for the center of the TC. These calculations, however, are generally performed using a single point as the TC center, whether it is from a model TC location algorithm (Marchok 2002; Walsh et al. 2007), from satellite location algorithms (e.g., Wimmers and Velden 2010), or from flight-level data (Willoughby and Chelmow 1982).

For finer details of TC core structure, vortex-scale analyses can include vortex tilt analyses (e.g., Jones 1995; Reasor and Montgomery 2001; Davis et al. 2008; Reasor et al. 2013; Stern and Zhang 2013), azimuthal Fourier wavenumber analyses (e.g., Reasor et al. 2009; Riemer et al. 2010), and near-core eddy interactions with the mean flow (e.g., Kwon and Frank 2008). These analyses have the potential to be extremely sensitive to center placement. Nguyen et al. (2014) used a single

Corresponding author address: David R. Ryglicki, Naval Research Laboratory, 7 Grace Hopper Ave., Stop 2, Rm. 254, Bldg. 704, Monterey, CA 93940.
E-mail: david.ryglicki.ctr@nrlmry.navy.mil

DOI: 10.1175/JAMC-D-15-0125.1

ARW simulation to demonstrate some differences in diagnosed centers. They found that the pressure centroid calculation yielded the smoothest results in both time and in the vertical direction for their simulation while also indicating that winds at a farther radius beyond the RMW should be calculated for stability. Ryglicki (2015) demonstrated how, for an idealized barotropically unstable vortex, some potential vorticity (PV) centroids can become unstable and erratic during times of maximum mixing. They also demonstrated how components of their eddy energy equation and Fourier amplitudes vary when changing the center.

Many previous works have attempted to calculate the center of model TCs using a variety of methods, as explored in Ryglicki and Hart (2015, hereinafter RH15). RH15 presented an expanded analysis of center-finding method differences. They divided center-finding methods into three distinct classes: local extreme (LE), weighted grid point (WGP), and minimization of azimuthal variance (MAV). They showed how the spread of these centers increases at higher levels in the storms. They also demonstrated that the spread of the centers shows an interesting relationship with intensity, as the spread of the centers remains small for storms whose low-level maximum mean tangential wind (MMTW) speed is greater than $33\,\mathrm{m\,s^{-1}}$ (RH15, their Figs. 6 and 7). These results were consistent across the three models that they analyzed: Coupled Ocean–Atmosphere Mesoscale Prediction System (COAMPS) TC model (hereinafter COTC; Doyle et al. 2012), the Hurricane Weather and Research Forecasting (HWRF) Model (Gopalakrishnan et al. 2012), and the Geophysical Fluid Dynamics Laboratory (GFDL) TC model (Bender et al. 2007). It was found that the spread of the centers can be manifested in a variety of ways, such as in cylindrical wind conversions and in vertical tilt magnitude and direction calculations. These are the first works that sought to analyze differences between different methods explicitly, as implications for center placement errors have only been alluded to in various previous works (e.g., Willoughby 1992; Marks et al. 1992; Jones 1995; Frank and Ritchie 1999, 2001; Cram et al. 2007; Reasor et al. 2013).

This work will seek to expand the analyses presented by RH15 by providing a more in-depth analysis of the possible inconsistencies that arise when using different center-finding methods on mature hurricanes. This work, Part I, will focus on low-wavenumber Fourier analyses and simple diagnostics (such as the RMW) at low levels. Part II (D. R. Ryglicki et al. 2016, unpublished manuscript) will focus on the three-dimensional structure and vertical tilt. Reasor et al. (2009) showed low-level Fourier analyses of vorticity in Hurricane Guillermo (1997), where the center was defined using the Hurricane Research Division's (HRD) simplex method (Marks et al. 1992), and noted a prominent wavenumber 2 feature. Kwon and Frank (2008) computed eddy energy calculations and indicated that, as opposed to a barotropic vortex (Kwon and Frank 2005), the primary energy transfer is mean potential energy to mean kinetic energy, but the center is implied to be a pressure minimum and not explicitly stated. Riemer et al. (2010) used a PV centroid with a weighting box of 120 km × 120 km and noted a prominent wavenumber 1 feature in the vorticity field of their sheared tropical cyclone. These are just some examples of different ways centers are defined and then used to calculate different metrics. This is certainly not to say, however, that any of the above methods are correct or incorrect. Indeed, RH15 pointed out that the most important condition for defining a center is fulfilling a need or answering a question posed. Ryglicki (2015) addressed this problem by showing how terms in their barotropic eddy energy equation and how the tilt itself could vary wildly merely by choosing between two different centers (their Fig. 19). This notion that different physical definitions for the location of a center will identify different locations in the TC is supported by observations. For example, Black et al. (1972) noted that at upper levels in their observed hurricanes, there existed two different centers—a pressure center and a circulation center.

Low-wavenumber Fourier analyses have important implications when attempting to diagnose vortex structure. For example, wavenumber 0 mean tangential wind is most often presented as the RMW, but wavenumber 1 vorticity could indicate a beta gyre (Wang and Holland 1996); wavenumber 1 radial wind and wavenumber 1 vorticity could indicate cross-vortex flow (Braun and Wu 2007) or a response to vertical shear (Riemer et al. 2010); wavenumber 2 vorticity could be used as a measure of eye or eyewall ellipticity (Reasor et al. 2009); and wavenumbers 3, 4, or 5 could be used to determine the polygonal shape of an eyewall (Schubert et al. 1999, hereinafter S99). These are just some of the ways that low-wavenumber Fourier analyses could be used to assess a vortex's structure. To assess the implications of different centers on diagnostic analysis, some of the analyses of RH15 will be expanded in section 2. Section 3 will discuss the methodology and the idealized profiles used for this research. Section 4 will present the results of the idealized profiles. Section 5 will present conclusions and a discussion, including implications for future analyses.

2. Expanded analysis of RH15

To frame the argument for this particular problem properly (i.e., low-wavenumber analyses and the diagnostics), the spread analysis of RH15 will be readdressed.

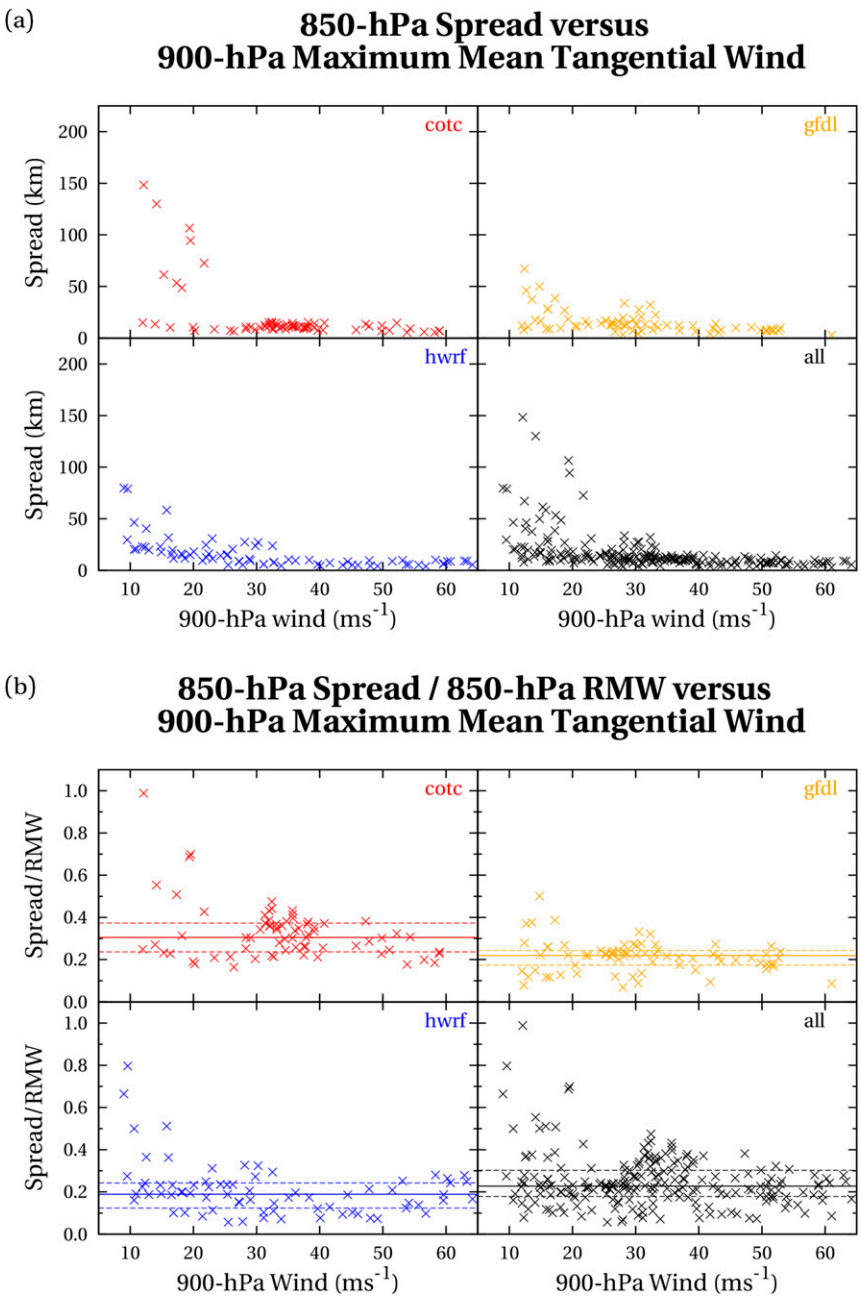

FIG. 1. (a) Absolute and (b) relative 850-hPa spread of the centers with respect to intensity. In (b), solid lines are the medians and dashed lines are the interquartile ranges.

Figure 1a shows the spread of the centers using the dataset from RH15 at 850 hPa, where spread is calculated as

$$s(z,t) = \sqrt{\frac{1}{M}\sum_{m=1}^{M}[\Delta_m(z)]^2}, \qquad (1)$$

where s is the spread, z is the vertical level, t is the forecast lead time, M is the total number of methods, m is the method, and Δ_m is the Euclidean distance between a calculated center and the mean of the centers for a given height and forecast lead time. As a reminder, the RH15 dataset includes simulations of 2012 hurricanes Debby (Atlantic Ocean), Daniel (east Pacific Ocean), and Emilia twice (east Pacific) in HWRF, COTC, and GFDL for a total of 219 forecast times. Table 2 of RH15, which catalogs all of the center-finding methods used there, is imported here as Table 1.

TABLE 1. Center-finding methods used in RH15 and discussed in this paper. DOF is degrees of freedom, and abbrev gives the abbreviations and acronyms used in the text and figures to label the methods. This table is reproduced in its entirety from Table 2 of RH15.

Method	Class	DOF	Abbrev
Tangential wind max, height min first guess, brute force in 5 × 5 gridpoint search area	MAV	4	MAVWB
Tangential wind max, height min first guess, brute force in 5 × 5 gridpoint search area, then simplex (maintain RMW and annulus), 30 iterations to convergence	MAV	5	MAVWBS
Tangential wind max, height min first guess, simplex, 30 iterations	MAV	5	MAVWZMS; MAV WHMS
Tangential wind max, center of domain first guess, simplex, 30 iterations	MAV	5	MAVWCS
Height min	LE	3	ZMIN; HGT Min
Height ring, height min as first guess, 100 × 100 gridpoint subdomain, varying annulus	WGP	5	ZRING; HGT Ring
PV centroid, 60 km × 60 km weighting area, height min first guess, 10 iterations to convergence	WGP	4	PVC060060; PV Cent. 60x60
PV centroid, 120 km × 120 km weighting area, height min first guess, 10 iterations	WGP	4	PVC120120; PV Cent. 120x120
PV centroid, 300 km × 300 km weighting area, height min first guess, 10 iterations	WGP	4	PVC300300; PV Cent. 300x300
PV centroid, entire domain as weighting area	WGP	4	PVCONCE; PV Cent. Domain
PV max	LE	3	PVMAX

Despite the fact that the signal is not quite as distinct at 850 hPa as it is at 500 and 300 hPa (RH15, their Figs. 6 and 7), Fig. 1a shows that a dependence on intensity still exists even at lower model levels. Here, intensity is defined as the MMTW (the value of the mean tangential wind at the RMW) at 900 hPa as calculated using the HRD's simplex method after applying the brute force method (MAVWBS). This analysis is presented, however, in an absolute sense. Figure 1b presents these data again displayed in a relative sense, as the ordinate is now spread of the centers normalized by the RMW at 850 hPa as calculated from the MAVWBS technique. Unless a storm is incredibly weak, the normalized spread does not show the same signal against intensity as the spread alone does in an absolute sense. In fact, the median spread/RMW value for the entire dataset at this level is approximately 0.225. The question then becomes, how much does this ratio matter, if at all?

Figure 2 is a snapshot of eastern Pacific Hurricane Emilia (initialized 1200 UTC 10 July 2012) in HWRF at forecast hour 6 at the 850-hPa level. It appears from this image that most of the centers are packed closely together, except for PVMAX and perhaps PVCONCE (all method abbreviations used in this paper are defined in Table 1). PVC060060 is farther to the south than the others clustered together. The normalized spread of these centers is approximately 0.29. To investigate how this spread might manifest itself with respect to RMW characteristics and to Fourier analyses, the storm fields–PV, zonal wind, and meridional wind—are first interpolated to a cylindrical grid using Lagrange polynomial bicubic interpolation. The cylindrical grid has a radial grid spacing of 2 km and 64 points in the azimuth. For reference, the horizontal grid spacing of this HWRF simulation is 3 km. The Cartesian winds are then converted to cylindrical winds on this new grid. Figure 3a is the RMW and the MMTW for each of the 12 centers used in RH15 at 850 hPa. Given the fact that the MAV techniques seek to optimize the RMW itself, it stands to reason that some of these centers from this particular technique will have the largest MMTW: 62 m s^{-1}. Figure 3b is the same information as Fig. 3a, but normalized by the MMTW and the RMW of the MAVWBS method. If we assume that the MAVWBS is as close to the optimal location of the RMW as possible (RH15, p. 830), then from these figures, it would appear that the sensitivity of the MMTW is less than that of the RMW, given how even at farther distances of PVCONCE and PVMAX, the MMTW does not decrease by the same factor. This will be explored more thoroughly in section 4. Additionally, the MAV techniques, by maximizing the MMTW, appear to result in the calculation of the smallest RMW.

In addition to MMTW and RMW diagnostics, higher-order analyses that have been used to reveal details about the structure of TCs are low-wavenumber azimuthal Fourier analyses (e.g., Riemer et al. 2010; Reasor et al. 2009). RH15 showed how, even for the same storm, qualitative and quantitative analysis of cylindrical wind fields can be greatly affected by the positioning of the center. RH15 demonstrated that radial wind variances occur over the breadth of the storm itself, while tangential wind differences are generally located in the inner core (RH15; Figs. 9–11). Figure 4 shows the low-wavenumber (0,1, and 2) Fourier amplitudes of PV (Fig. 4a), tangential wind (Fig. 4b), and radial wind (Fig. 4c) of HWRF TC Emilia at 850 hPa. While these images present a plethora of information, only the most salient features will be discussed.

Figure 4a indicates that PV variability seems to exist most prominently at radii between 10 and 30 km.

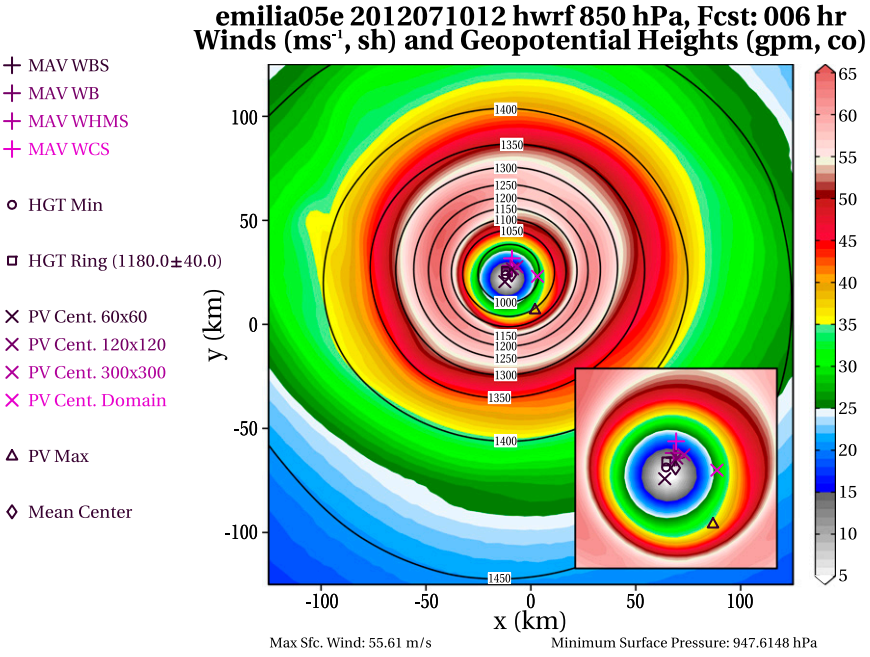

FIG. 2. Centers of Hurricane Emilia at 850 hPa in HWRF at forecast hour 6. Winds are given by the colored shading, and heights are given by contours. Inset is zoom of the inner core.

MAVWBS would indicate two peaks of PV in the mean—one near 15 km and another near 26 km. MEANC, ZMIN, ZRING, and PVC060060 do not show this bimodal structure, instead placing a peak of vorticity at a radius of approximately 20 km. These differences also cascade to higher wavenumbers. For example, MAVWBS would indicate a wavenumber 1 asymmetry at 26 km, whereas PVC060060 eliminates this feature almost completely in lieu of a wavenumber 1 asymmetry farther out radially at 36 km and a wavenumber 2 asymmetry at approximately 28 km.

Tangential wind and radial wind differences are presented in Figs. 4b and 4c. With the exception of PVMAX (which is essentially an outlier), the mean tangential wind structure is generally similar among all methods. Most of the differences occur in the wavenumber 1 asymmetry field between 0 and 30 km. There also exist subtle, small differences in the wavenumber 2 asymmetry field, but most of the methods indicate a very weak signal ($\sim$1 m s^{-1}) at 36 km. The radial wind differences, however, are very striking. It would appear that radial flow is not significant in a mean sense at 850 hPa, but the wavenumber 1 asymmetries show much greater variability. The MAVWBS method would indicate that there exists cross-vortex flow between 0 and 35 km at magnitudes ranging from approximately 10 to 5 m s^{-1}. MEANC displays a notable gap in this flow at 32 km and replaces it with a stronger asymmetry at 50 km. An analysis based on PVC060060 would reduce the flow at innermost radii (0–20 km), but it would also indicate a stronger radial flow asymmetry at 40–60 km. Figure 5 shows the interpretations of radial wind for this level and time in HWRF using the 12 centers investigated in RH15. Some of them are subtly different (MAVWB and MAVWBS); some are noticeably different (MAVWCS and PVC060060).

3. Idealized vortex construction

Evidently, there is much nuance and inconsistency in performing Fourier analyses and diagnostics using different centers. Additionally, the HWRF simulations are notably complex from a numerical perspective since they include a host of diabatic processes, external forcings, and additional parameterizations. It is for these reasons that we choose to perform our center-position error analysis on idealized vortices. It is not clear that there is even a ''best'' or ''correct'' center based on previous work (RH15). If we create idealized 2D vortices, we automatically know what the ''correct'' solution to the problem is, and we can hopefully extrapolate those experiences to models of higher complexity. Two parametric, prescribed profiles were chosen to construct the idealized vortex profiles throughout the rest of this work. The first profile is a wind-based parametric profile (Willoughby et al. 2006, hereinafter WDR);

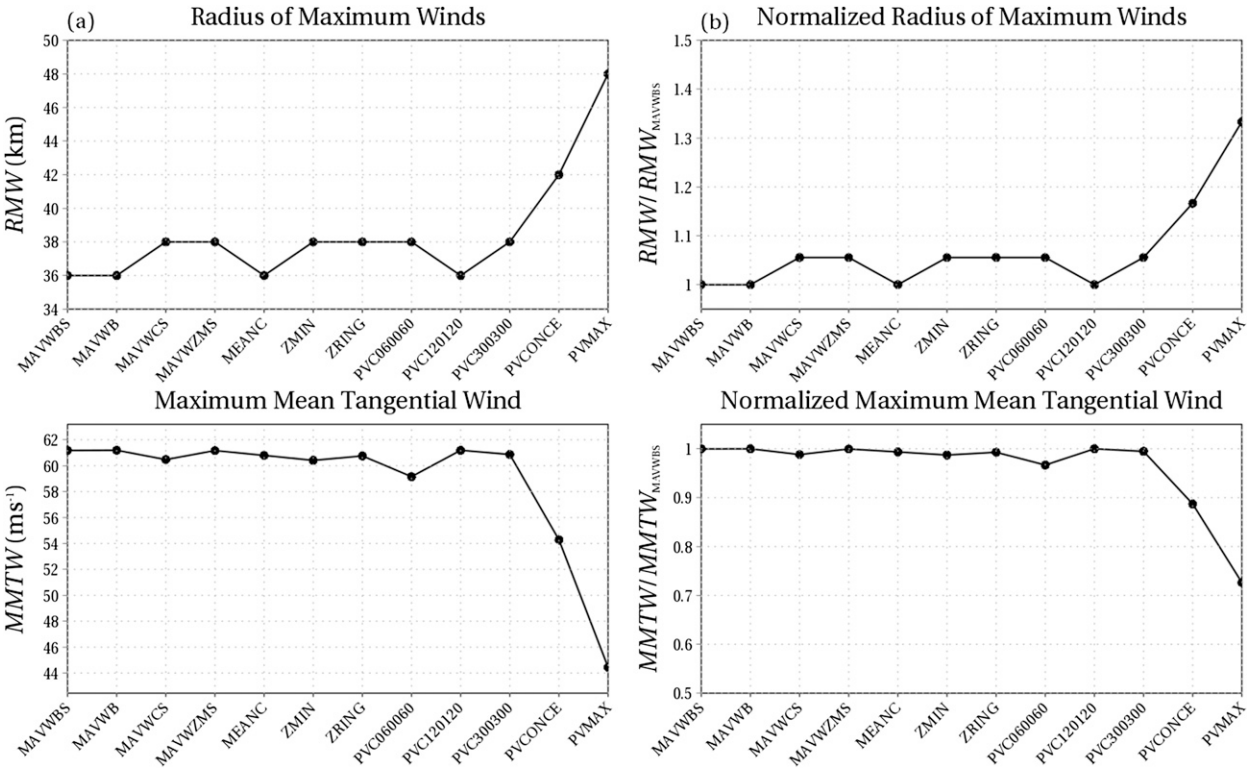

FIG. 3. (a) RMW and MMTW and (b) normalized RMW and MMTW for forecast hour 6 of Hurricane Emilia in HWRF at 850 hPa.

the second profile is a vorticity-based parametric profile (S99).

The WDR profile (dual exponential) is defined as

$$\overline{V}(r) = V_i = V_{\max}\left(\frac{r}{R_{\max}}\right)^n, \quad 0 \le r \le R_1, \tag{2a}$$

$$\overline{V}(r) = V_i(1-w) + V_O w, \quad R_1 < r < R_2, \quad \text{and} \tag{2b}$$

$$\overline{V}(r) = V_O = V_{\max}\left[(1-A)\exp\left(-\frac{r-R_{\max}}{X_1}\right) + A\exp\left(-\frac{r-R_{\max}}{X_2}\right)\right], \quad r \ge R_2, \tag{2c}$$

where n, $R_{\max}$, R_1, R_2, A, $V_{\max}$, X_1, and X_2 are prescribed constants; r is the radius; and w is a bellramp transition function that is defined as

$$w(\xi) = 126\xi^5 - 420\xi^6 + 540\xi^7 - 315\xi^8 + 70\xi^9, \tag{3}$$

which is expressed in terms of a nondimensional variable,

$$\xi = \left(\frac{r-R_1}{R_2 - R1}\right). \tag{4}$$

The specifics of solving for w and the profile itself are explained in WDR. For all of the profiles in this work that use the WDR profile, $V_{\max}$; $R_{\max}$; n; A; X_1; X_2; and the denominator of Eq. (4), the width of the blend zone, are all prescribed. The w is then obtained numerically using Newton's method, with a convergence threshold of 1×10^{-6}, following the methods outlined in WDR to get R_1 and R_2. The S99 profile is defined as

$$\overline{\zeta}(r) = \begin{cases} \zeta_i & r_{i-1} + d_{i-1} \le r \le r_i - d_i \\ \zeta_i S[(r - r_i + d_i)/2d_i] + \zeta_{i+1} S[(r_i + d_i - r)/2d_i] & r_i - d_i \le r \le r_i + d_i \\ \zeta_{i+1} & r_i + d_i \le r \le r_{i+1} - d_{i+1} \end{cases}, \tag{5}$$

where S is the Hermite polynomial $[S(s) = 1 - 3s^2 + 2s^3]$ and where r_i, d_i, and ζ_i are prescribed constants. The S99 profile is used when more exacting control of the vorticity field is desired.

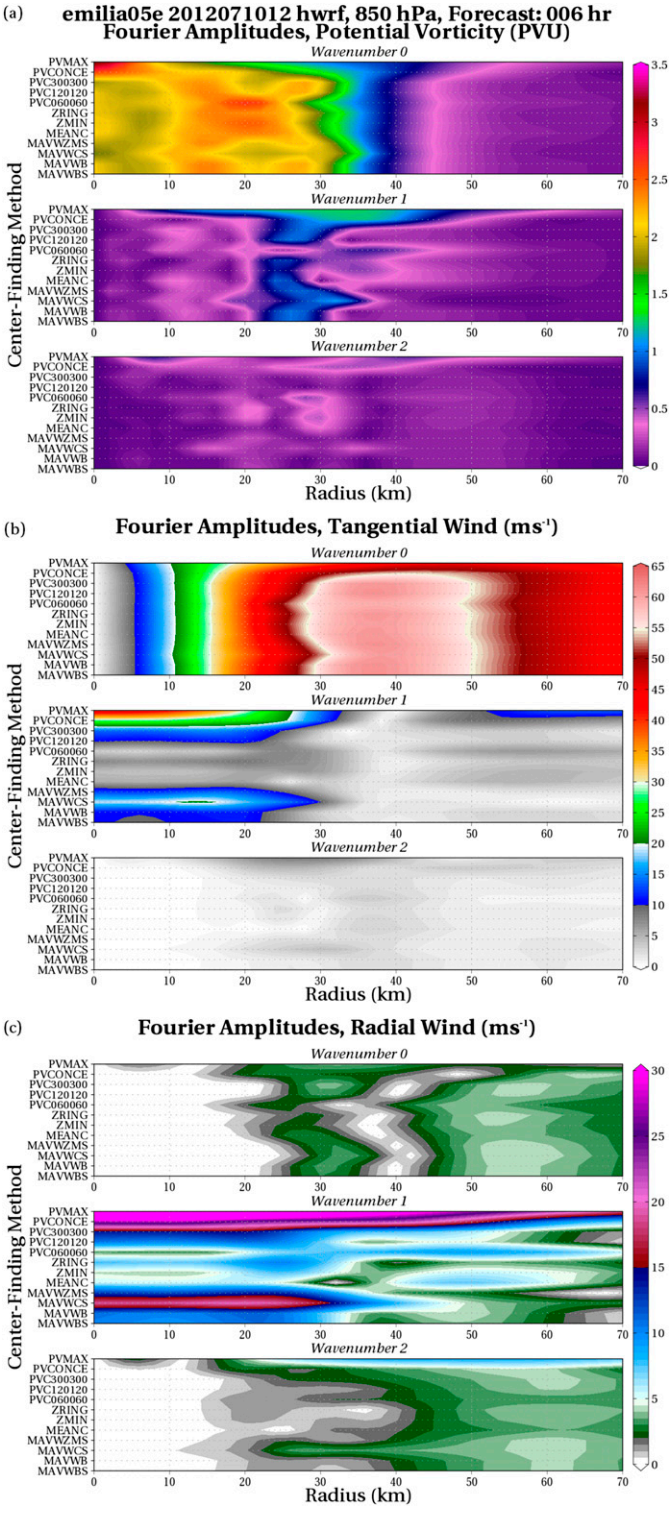

FIG. 4. Azimuthal Fourier amplitudes of (a) PV, (b) tangential wind, and (c) radial wind at 850 hPa for HWRF Hurricane Emilia.

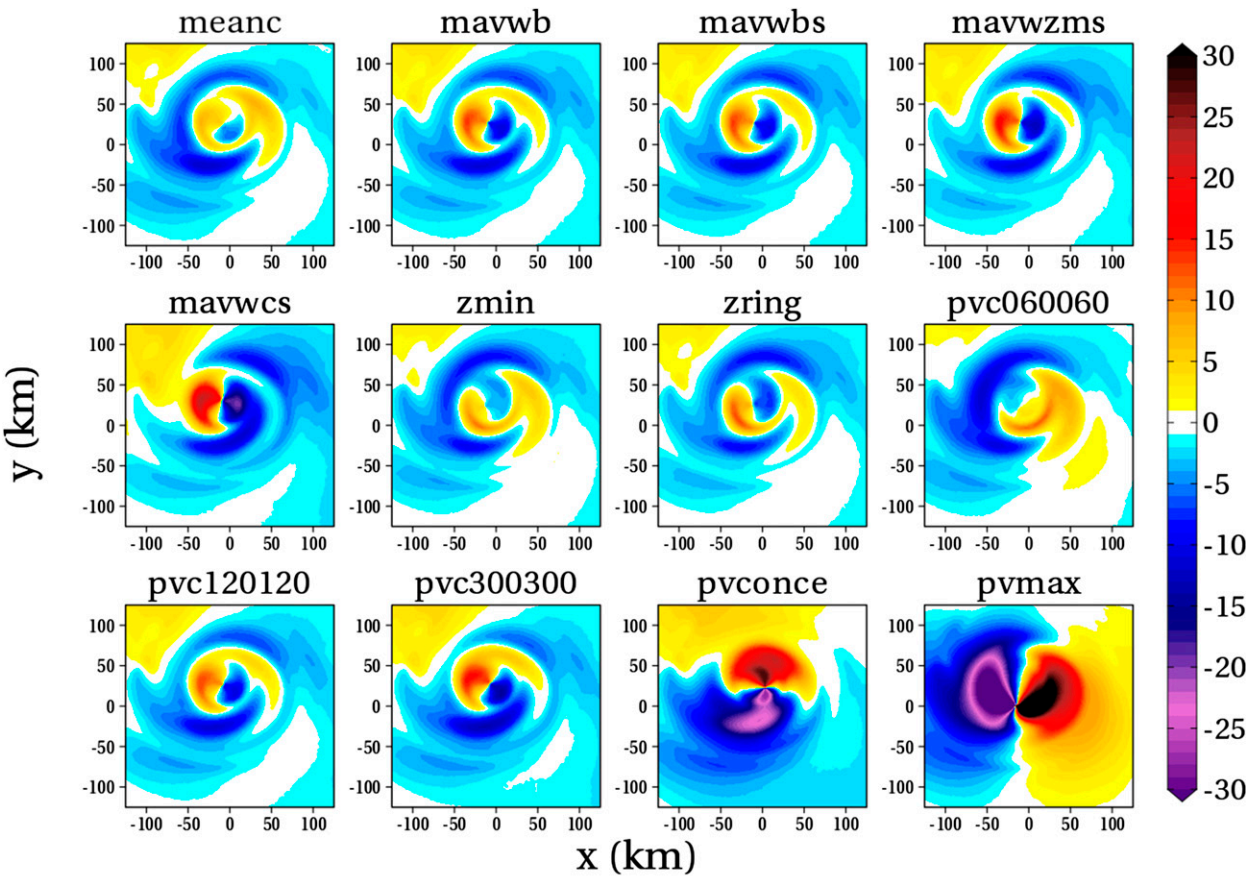

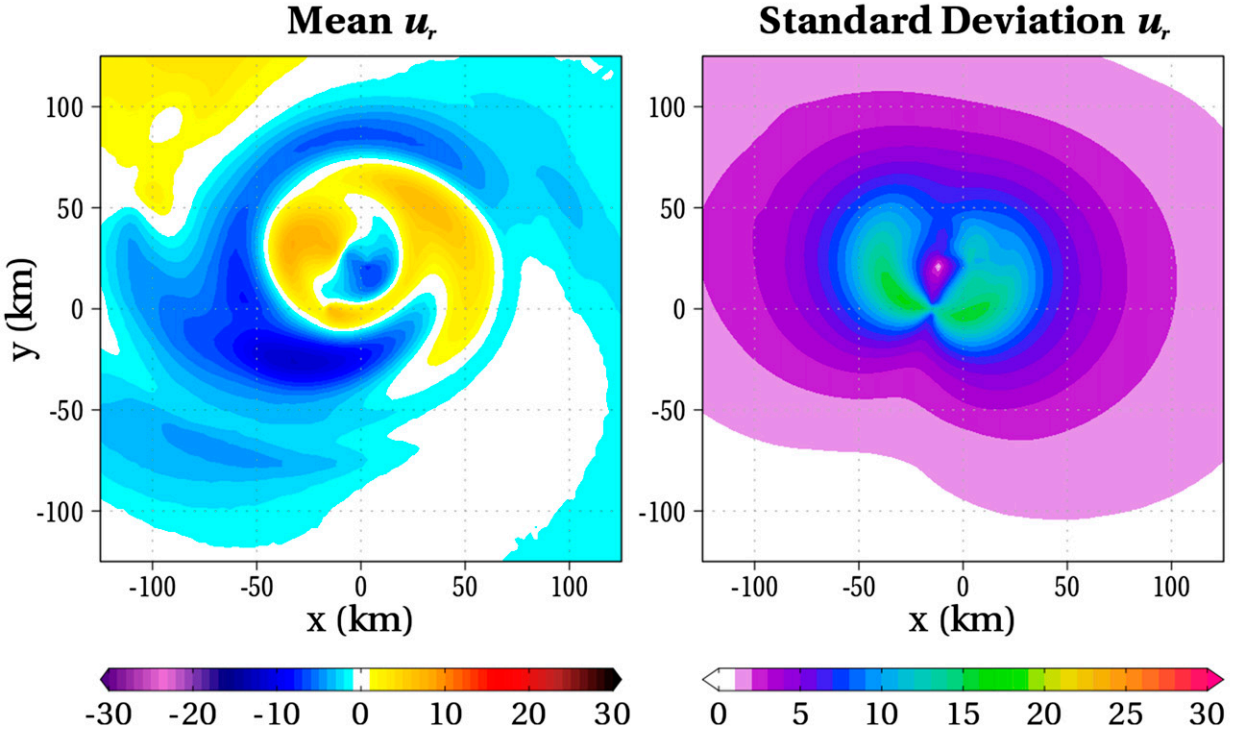

FIG. 5. (top three rows) Radial wind fields ($m\,s^{-1}$) for forecast hour 6 of Hurricane Emilia in HWRF at 850 hPa for each center, and the (bottom left) mean and (bottom right) standard deviation of those fields. Abbreviations can be found in RH15.

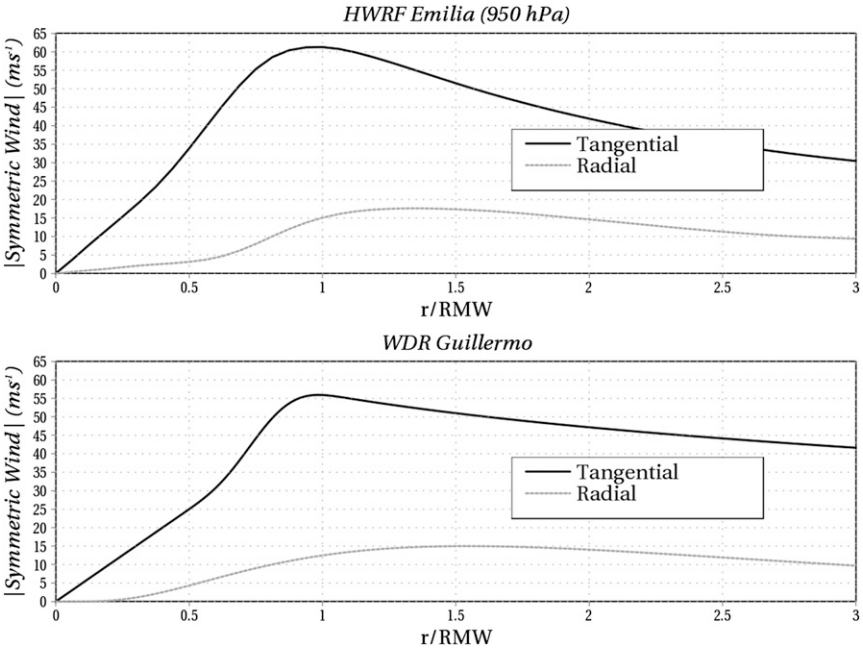

FIG. 6. Magnitudes of symmetric tangential and radial winds (top) for forecast hour 6 of Hurricane Emilia in HWRF at 950 hPa and (bottom) for a prescribed symmetric wind field based on Hurricane Guillermo with a prescribed lognormal radial wind field.

In cases in which a symmetric radial wind profile is desired, a lognormal function is used. The radial wind is prescribed as

$$\overline{U}(r) = \frac{U_{\max}}{r} \exp\left\{ s - \frac{t^2}{2} - \left[\frac{(\ln r - s)^2}{2t^2} \right] \right\}, \qquad (6)$$

where $U_{\max}$ is the maximum radial wind and s and t are prescribed constants. The details of the derivation of this equation can be found in appendix A. The reason why a lognormal function is used for radial wind is that, unlike tangential wind, where the wind profile generally is thought to be a power law in the core with an exponential decay at larger radii (Willoughby et al. 2006), there exists more debate about the radial structure of radial winds in a hurricane (Kepert 2006; Zhang et al. 2009; Montgomery et al. 2014). Often, when radial winds are presented, they are shown in boundary layer studies in the r–z plane (e.g., Kepert 2006; Montgomery et al. 2014). The simple parameterization here does not account for return flow from the eye due to, for example, supergradient winds, and it is presumed that the radial wind ceases between the RMW and the center of the vortex. As a comparison with a model, Fig. 6 shows the absolute value of the mean wind components from Emilia in HWRF at 950 hPa from the same forecast time as in Fig. 2. In HWRF Emilia, the radial wind profile peaks around 1.3 × RMW, while with the prescribed profile of a tangential wind field based on Hurricane Guillermo (Reasor et al. 2009), the peaked radial wind is located at 1.5 × RMW. We are not arguing that the lognormal function is a perfect fit to a radial wind profile, but we do believe that for our demonstrative purposes, this prescription is adequate.

All parametric profiles are initialized on a high-resolution cylindrical grid, where dr is 0.1 km and $d\lambda$ is $\pi/360$ radians. After the initial profiles are specified, the WDR profile is converted to vorticity. If asymmetries are to be added, the symmetric vorticity field is then converted to a streamfunction field by inverting the relation $\overline{\zeta}(r) = \nabla^2 \overline{\psi}(r)$, using the trapezoid rule twice and the boundary condition that the streamfunction vanishes far from the vortex. After the symmetric streamfunction has been calculated, Gaussian asymmetries are added in the form

$$\psi'(r,\lambda) = A' \exp\left[-\frac{(r-b)^2}{2c^2} \right] \cos[n(\lambda - \varphi)], \qquad (7)$$

where A' is the amplitude, b is the radial location of the asymmetries, c is the radial width, n is the wavenumber, λ is the azimuth angle, and φ is the phase angle. To mimic real eyewall perturbations, asymmetries are centered on the steep gradient of vorticity between the inner-core vorticity and the RMW (e.g., S99; Hendricks et al. 2009; Reasor et al. 2009). The perturbation radial

wind field, full tangential wind field, and full vorticity field are then derived from the full streamfunction field (with exceptions to be noted later). If a symmetric radial (irrotational) wind is to be added, it is added at this point. The cylindrical winds, regardless of perturbations, are converted to Cartesian winds on the cylindrical grid. These three fields—vorticity and the two Cartesian wind components—are then interpolated using bicubic interpolation to a Cartesian grid where $dx = dy = 2$ km. This grid spacing is meant to mimic some cloud-system-resolving simulations that use Cartesian domains (e.g., Braun and Wu 2007). It is on this grid where the center will be displaced. Unless otherwise noted, there will be 32 different centers—one at the true center, and then 31 intermediate centers between the true center and the RMW—spaced evenly apart. At each new center, the Cartesian grid is interpolated back to a cylindrical grid using bicubic interpolation, identical to section 2's HWRF analysis. The Cartesian winds are converted back to cylindrical winds at this point. While the two interpolations may result in the addition of small amplitude artificial noise, most of the analyses presented will be low wavenumbers (0–4), and the possible data degradation, we feel, is minimal in those wavenumbers.

4. Idealized analyses

a. *Idealized symmetric case study*

First and foremost, it should be stated that this work is not meant to examine every nuance of either the WDR profile or the S99 profile. We will attempt, however, to be clear as to how the vortices are prescribed. To gauge basic behavior of shifting the center on a symmetric vortex, the first vortex analyzed will be one whose parameters have already been fitted to an observational profile in WDR (their Fig. 2): Hurricane Diana (1984). Figure 7 shows the initial winds and the initial vorticity profile. The appeal of the dual-exponential WDR formulation [Eq. (2c)] is that it allows for a peaked vorticity profile inside the RMW and sharper wind gradients around the RMW itself, structures which observations indicate are present in mature storms (Mallen et al. 2005; Reasor et al. 2009; Hendricks et al. 2012). With the initial profile set, the center can be moved iteratively from the true center to the RMW. Figure 8 presents the normalized change in MMTW and RMW as the center is moved. The expansion of the RMW appears to be parabolic, as the RMW change at early offsets is small compared to later offsets. The decrease in MMTW, however, is much more gradual, indicating that displacement of the center will have a larger effect on the RMW's expanse than on its magnitude.

Figure 9 is a "postage stamp" plot that presents the normalized low-wavenumber Fourier amplitude error profiles of vorticity, tangential wind, and radial wind. The thin black line is the RMW calculated from that particular offset (it is a diagonally mirrored line for the RMW from Fig. 8). Wavenumber 0 radial wind shows the artificial noise from the two interpolations as discussed previously. The mean tangential wind decreases outward, mainly following the RMW, but there is also an increase in the mean at inner radii. The mean vorticity appears to bifurcate, as the maximum vorticity value moves radially inward and decreases in magnitude as the RMW increases outward.

Unsurprisingly, as the calculated center moves away from the correct center, aliasing errors increase. What is slightly unexpected is the structure and magnitude of these errors. While most of the aliasing occurs onto wavenumber 1, there is far more nuance to the problem than merely that fact. Tangential wind aliasing errors are largest inside the RMW with weaker signatures outside the RMW, while radial wind errors possess a much larger radial extent. For both tangential wind and radial wind, the errors become largest when the calculated center is farthest from the true center. The reason why radial wind errors appear so much larger in expanse is that radial wind aliasing errors are much more sensitive to displacement than tangential wind. Expressions, whose derivations are in appendix B, for relating the aliased errors of only the tangential winds are

$$v_t^n = v_t^o \cos(\theta_n - \theta_o) \quad \text{and} \tag{8a}$$

$$u_r^n = v_t^o \sin(\theta_n - \theta_o), \tag{8b}$$

where the superscripts and subscripts n and o indicate the components relative to a new center and an old center, respectively, and θ is the angle between a given grid point and a center location. In this case, the "old" center is the original, or true, center. Ultimately, since the sine function changes more rapidly with small changes in θ at small θ, the radial wind will be changed more rapidly than the tangential wind over the breadth of the storm. Tangential wind differences will be most apparent where θ changes are large—that is, closer to the moved center.

Vorticity asymmetries do not behave in this manner because of structural differences. The maximum vorticity asymmetries for wavenumbers 1–3 occur at 0.2 × RMW, 0.3 × RMW, and 0.35 × RMW, respectively. Additionally, in terms of absolute numbers, these maximum values (all $10^{-3}\,s^{-1}$) are 2.62, 1.41, and 1.05, respectively, when the mean value at these locations is between 3.0 and 4.0. It is important to remember that from Fig. 1b, the median normalized spread at 850 hPa for the entire dataset in RH15 is approximately 0.225, so it is entirely plausible that aliasing errors could play a

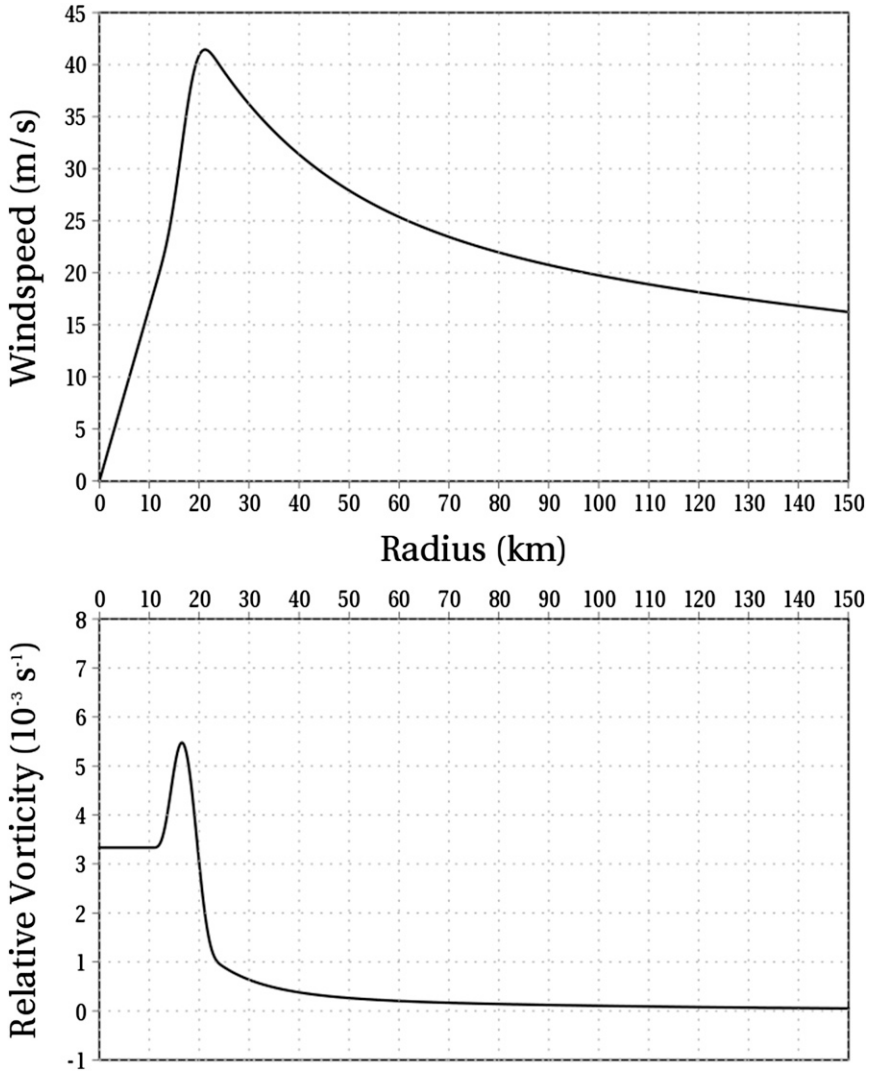

FIG. 7. Initial profiles of (top) wind and (bottom) vorticity for Hurricane Diana using the WDR method.

nontrivial role in Fourier analyses, especially when those analyses involve low-wavenumber vorticity.

It is important to keep in mind that these aliasing errors presented so far are from the symmetric mode only. There are many different aspects of a symmetric vortex that could affect the sensitivity of the aliasing—intensity of the vortex, size of the vortex, size of the RMW, and structure of the vortex, to name a few—but we will limit our discussion to those aspects that affect the aliasing the most. Additionally, we will address asymmetries and cross-vortex flow from a background wind field.

b. *Inner-core symmetric variations and isolated asymmetries*

First, we will examine how the inner-core peak vorticity profile affects aliasing. To address this feature directly, S99 profiles were used, as noted above, to exert more exacting control over the vorticity profiles. Figure 10 shows the eight profiles constructed using the S99 method. Four of the eight profiles maintain an inner vorticity value of $3.0 \times 10^{-3}\,s^{-1}$ and alter the values of the peak vorticity; four of them are shifted radially inward. While the outer wind structures are not as realistic as the exponential profile, they do not significantly alter the results of the findings presented here.

The normalized change in RMW and MMTW for all of the S99 profiles is shown in Fig. 11. These results indicate that RMW is much more sensitive to misplaced errors than is MMTW, which confirms the results seen from HWRF Emilia (Fig. 3). What is interesting is that regardless of the vorticity structure—and the resulting tangential wind structure—the error profile does not

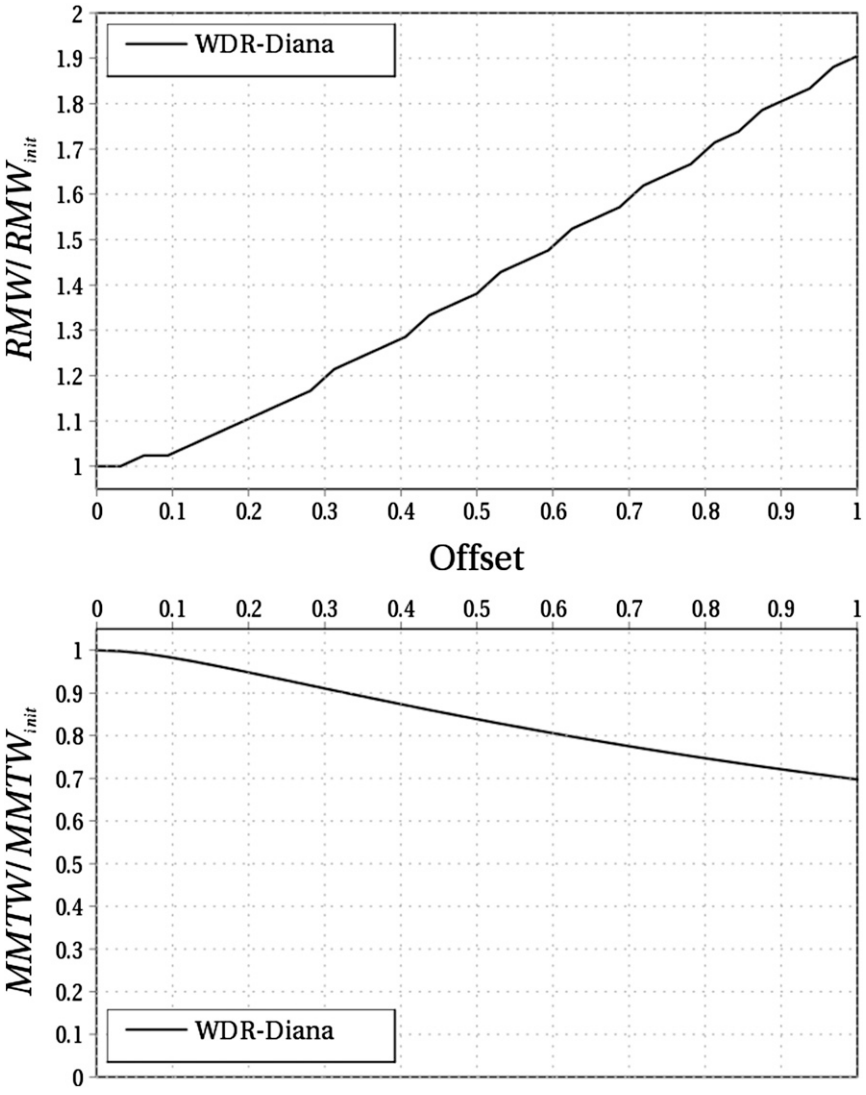

FIG. 8. WDR Diana normalized (top) RMW and (bottom) MMTW error profiles with increasing offset. Here, offset is the distance of the center from true center (offset = 0) to the RMW (offset = 1) normalized by the RMW.

appear to vary significantly. This test was performed with various more realistic WDR profiles, and the results are nearly the same (not shown). Ultimately, the only configuration that yielded the most deviance from the behavior shown here was one that used a single-exponential WDR profile. In that case, where the falloff of the winds outside the RMW is much more gradual than in the dual-exponential profiles, the MMTW drops much more slowly, with a 15% reduction in magnitude at maximum displacement. The RMW increases by 100% at the same distance.

For azimuthal Fourier amplitude differences, in a general sense, the errors expressed by the Diana experiment (Fig. 8) are consistent with the visualizations of errors of all of the S99 profiles tested here. The difference between the peak and the innermost core of vorticity is what adds nuance to the error structure. Figure 12 displays Fourier amplitudes of wavenumber 1 vorticity. If there is no peak of vorticity between the core and the outer regions of the vortex, then the aliasing pattern skews toward inner radii. If a vorticity peak is present, then larger asymmetries skew outward, following the shifting RMW. Additionally, there is an inner lobe of aliased error when a peak is present. When looking at radial wind errors, as shown in Fig. 13, the changing inner core profile causes an increase in radial wind error that seems to move with the inward-moving vorticity error.

Altering the radial size of the vortex alters the size of the errors spatially. Focusing on the vorticity field,

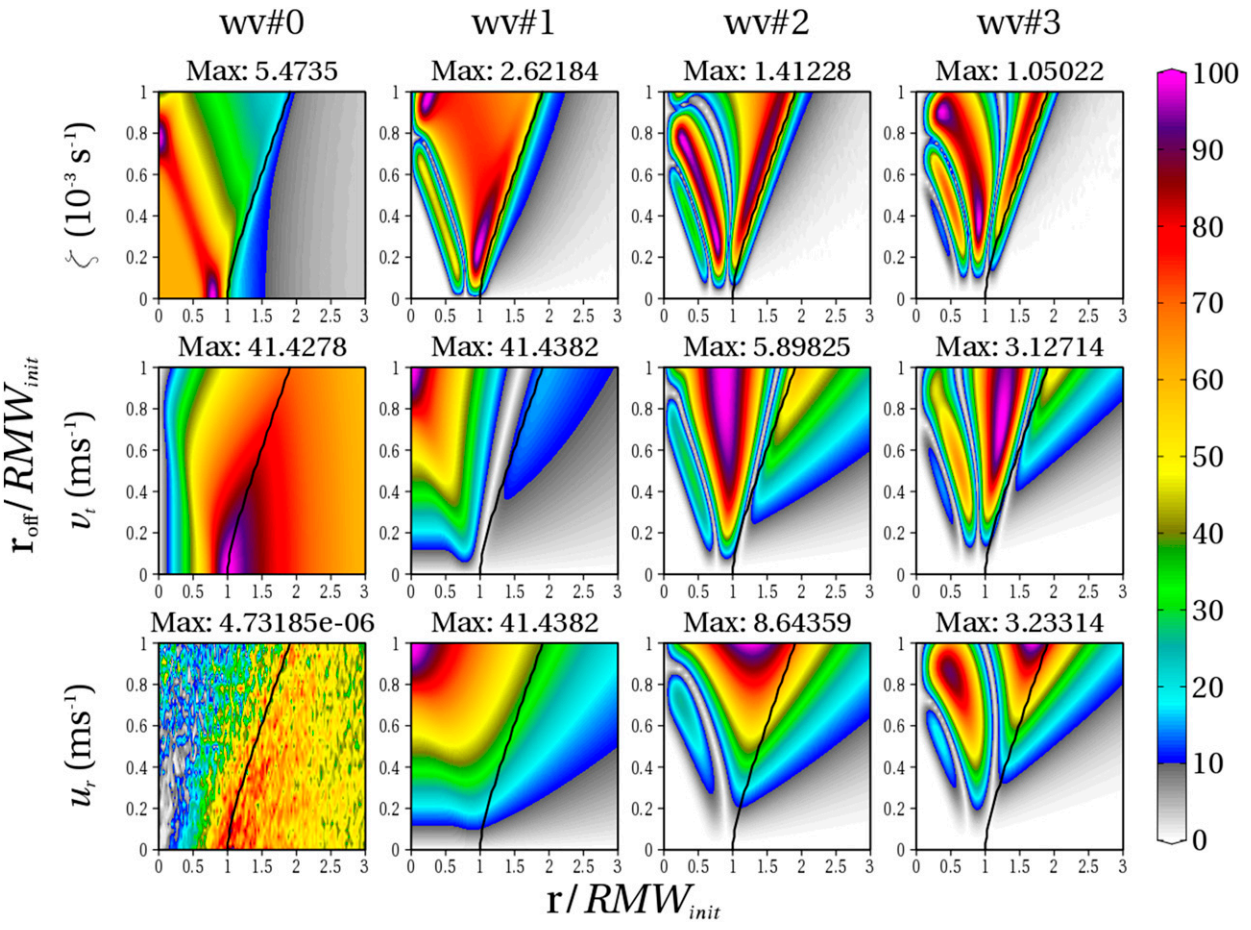

FIG. 9. Error profiles of normalized low-wavenumber Fourier amplitudes of vorticity, tangential wind, and radial wind for the WDR Diana profile for wavenumbers 0–3. Ordinate values are the offset value of the center with respect to the true center, and abscissa values are the value of the radius with respect to the original RMW. The black line is the RMW for that offset (i.e., inverted from Fig. 8).

Fig. 14 compares the large peak and the small peak vortices with their inward-shifted counterparts. The aliasing errors are of the same magnitudes for the peak values, but the offsets over which the errors are largest is greater when the vortex is smaller. This would indicate that for small storms whose winds, and thus vorticity, are very peaked, there is a smaller margin for error when calculating the center to prevent aliasing errors.

Having looked at how variations of the inner-core symmetric profile affect the aliasing error profile, we will now investigate the aliasing error profiles of asymmetric structures. To isolate the aliasing errors of the asymmetries, the symmetric vortex profile will be removed after the RMW has been calculated so the asymmetries can be placed properly. Ultimately, the characteristics that determine the structure of aliasing errors are not only the size and the strength of the asymmetries but also the location of the center placement relative to the asymmetry. Figure 15 shows an example of this structure in the vorticity field. In all cases, the wavenumber 1 asymmetry is located in the same spot. What is different is how the centers are moved. They are moved toward the maximum of the asymmetry, toward the minimum of the asymmetry, or along the zero contour of the wavenumber 1 vorticity asymmetry. In this case, if the center is moved along the axis either toward or away from the maximum, then there exist dual lobes that extend both radially inward and outward. If the center is positioned at any point on the zero axis, the information loss is more gradual before bifurcating. This behavior is consistent with all other visualizations for other wavenumber asymmetries, except that the aliasing lobes become more numerous with higher wavenumbers as the center placement drifts from the true center (not shown). Figure 16 shows how the wavenumber asymmetries, where the center drift is shifted along the zero axis, alias onto other low wavenumbers in isolation. Most of the aliasing cascade is to higher wavenumbers (not shown). Changing the radial size and magnitude of the asymmetry will alter its characteristic error profile accordingly, but the general behavior is

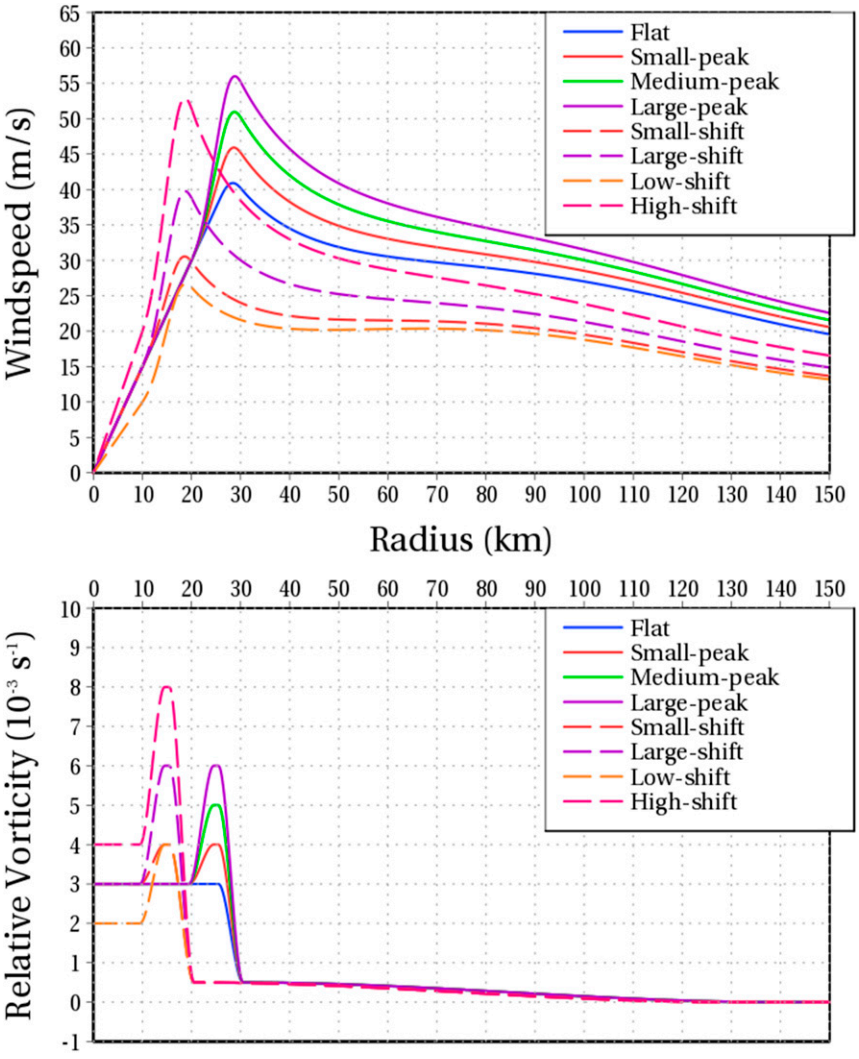

FIG. 10. Initial (top) wind and (bottom) vorticity profiles of the eight S99 vortices.

similar to what is seen here—wavenumber asymmetries generally yield dual lobes at other wavenumbers as displacements increase. Note that when applied to a full vortex, the RMW and MMTW error profiles do not change (not shown). When multiple asymmetries constructively interfere and become large enough, as will be explored in section 4d, they will begin to alter those diagnostic error profiles.

c. *Symmetric tangential and radial winds*

As was shown previously in section 4a, the aliasing of the mean tangential wind primarily affects inner-core vorticity and wavenumber 1 radial winds. While a strong, symmetric radial inflow is not relevant for the middle levels of a mature storm (Montgomery et al. 2014, cf. their Fig. 3), it is certainly relevant for lower levels of the storm (Kepert 2006, cf. his Fig. 5). A symmetric radial wind profile was added to the WDR Diana in a similar fashion as the one seen in Fig. 5. The postage-stamp plot of error profiles can be seen in Fig. 17; however, on the top row, vorticity has been replaced with divergence. Since symmetric tangential wind is derived via the streamfunction, it is purely nondivergent. The symmetric radial wind is derived via the velocity potential and is thus purely irrotational. The aliasing of the symmetric radial wind onto vorticity is negligible akin to how the aliasing of the symmetric tangential wind onto divergence is also negligible (not shown).

What is most interesting here is how the purely symmetric field is aliased onto other components of the storm. In comparing Fig. 17 with Fig. 9, the wavenumber 1 radial wind field does not appear sensitive to the symmetric radial wind field at all. Indeed, for this radial wind profile, the maximum difference between the profile with

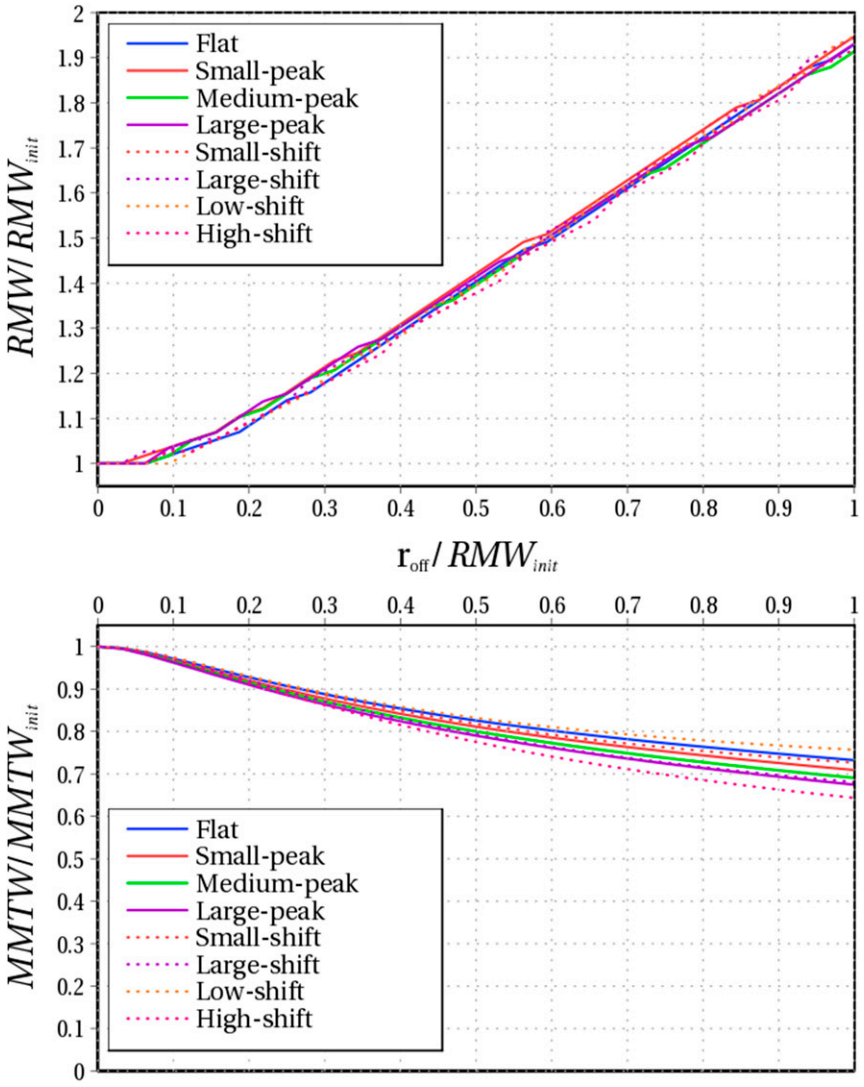

FIG. 11. Normalized error profiles of (top) RMW and (bottom) MMTW with offset centers for the S99 vortices.

the radial wind and without is only 1.75 m s^{-1}, and that only occurs when the center is offset to the original RMW (not shown). Furthermore, the most significant aliasing occurs onto wavenumber 1 of tangential wind in the gap between the two lobes seen in Fig. 9.

d. Symmetric tangential and radial winds with multiple inner-core asymmetries and a background flow

For this section, which comes the closest to what might actually be found in a modeled storm, a new profile is used. The symmetric profile and the asymmetries for this subsection are based on observational records of eastern Pacific Hurricane Guillermo from 1997 (Reasor et al. 2009; Reasor and Eastin 2012). The magnitudes of the asymmetries are provided, but the phases are not (cf. Figs. 15 and 16 from Reasor et al. 2009). For this particular section, the zero axes of all of the perturbations are coincident. A -5 m s^{-1} straight-line background zonal flow is added, and the same symmetric radial wind field from section 4c is added. The full profile can be seen in Fig. 18. The lobes on either side of the perturbation vorticity maxima are due to the prescription of the vorticity from the Gaussian streamfunction perturbation. Guillermo appeared to have a much broader wind profile than Diana. The RMW and MMTW change is not noticeably different from what was shown for the varying inner-core vorticities of the S99 profiles when considering only the symmetric component; however, what does alter the

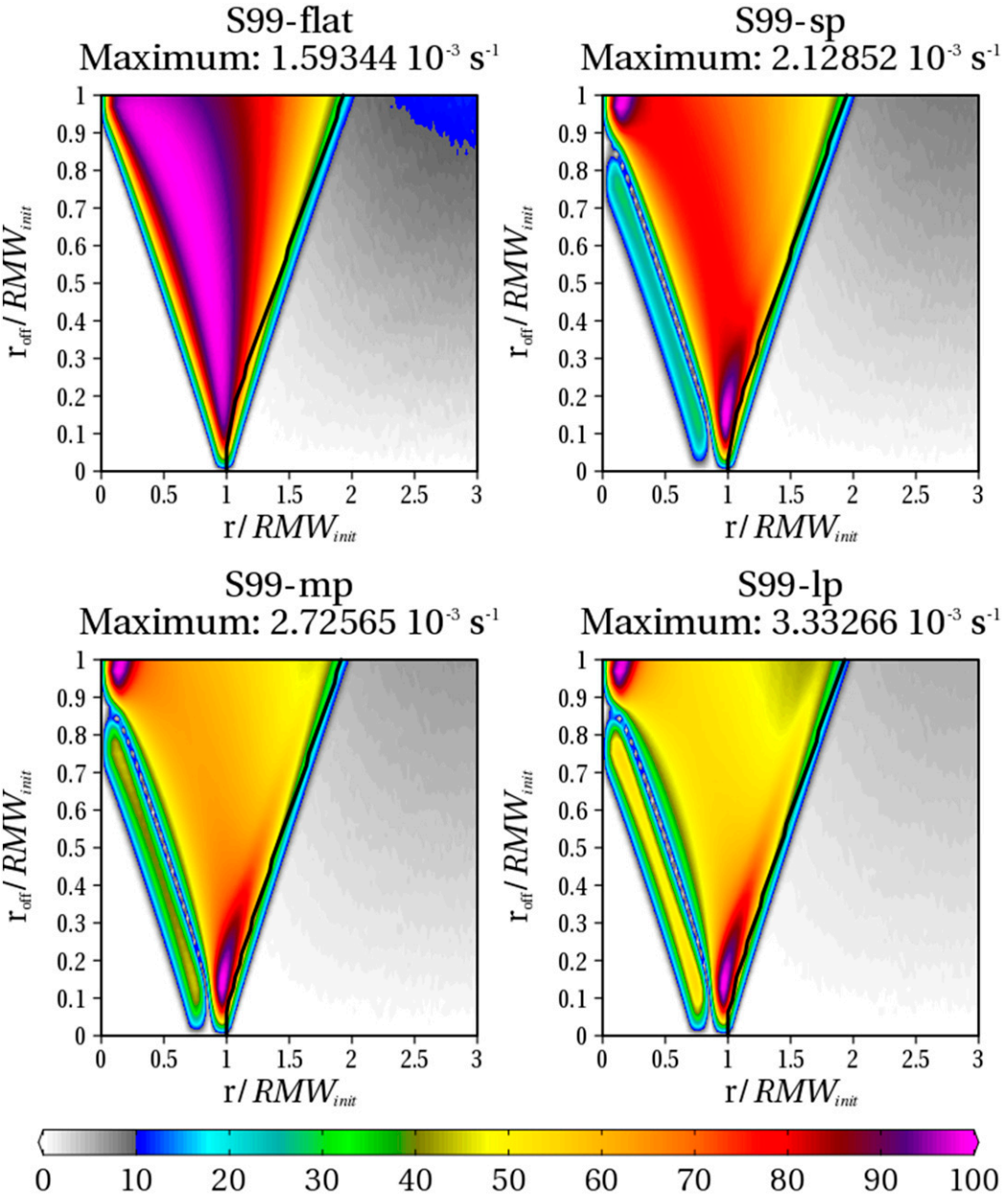

FIG. 12. Normalized wavenumber 1 azimuthal Fourier amplitudes of vorticity for the S99 vortices: no peak (S99-flat), small peak (S99-sp), medium peak (S99-mp), and large peak (S99-lp).

RMW and the MMTW error profiles is the position of the asymmetry relative to the center position. Three separate profiles were analyzed for this particular case, all of which maintained the same amplitudes of the perturbations but shifted the phases in unison. These can be seen in Fig. 19.

Figure 20 shows the change in RMW and MMTW of the three final profiles plus only the symmetric profile. All of the centers are moved due northeast from their original starting positions. The overall decrease in MMTW is less than that for WDR Diana (Fig. 7) because of the slower fall-off of the winds outside the core relative to the peak wind. What is most surprising about this is how different the RMW values are at even low values of the offset. When the center is moved directly toward the largest asymmetry, the RMW change is virtually the same to just the symmetric profile. Conversely, if the center is moved parallel to the maximum asymmetry, the RMW decrease does not occur until an offset of 0.12. If the center is moved away from the

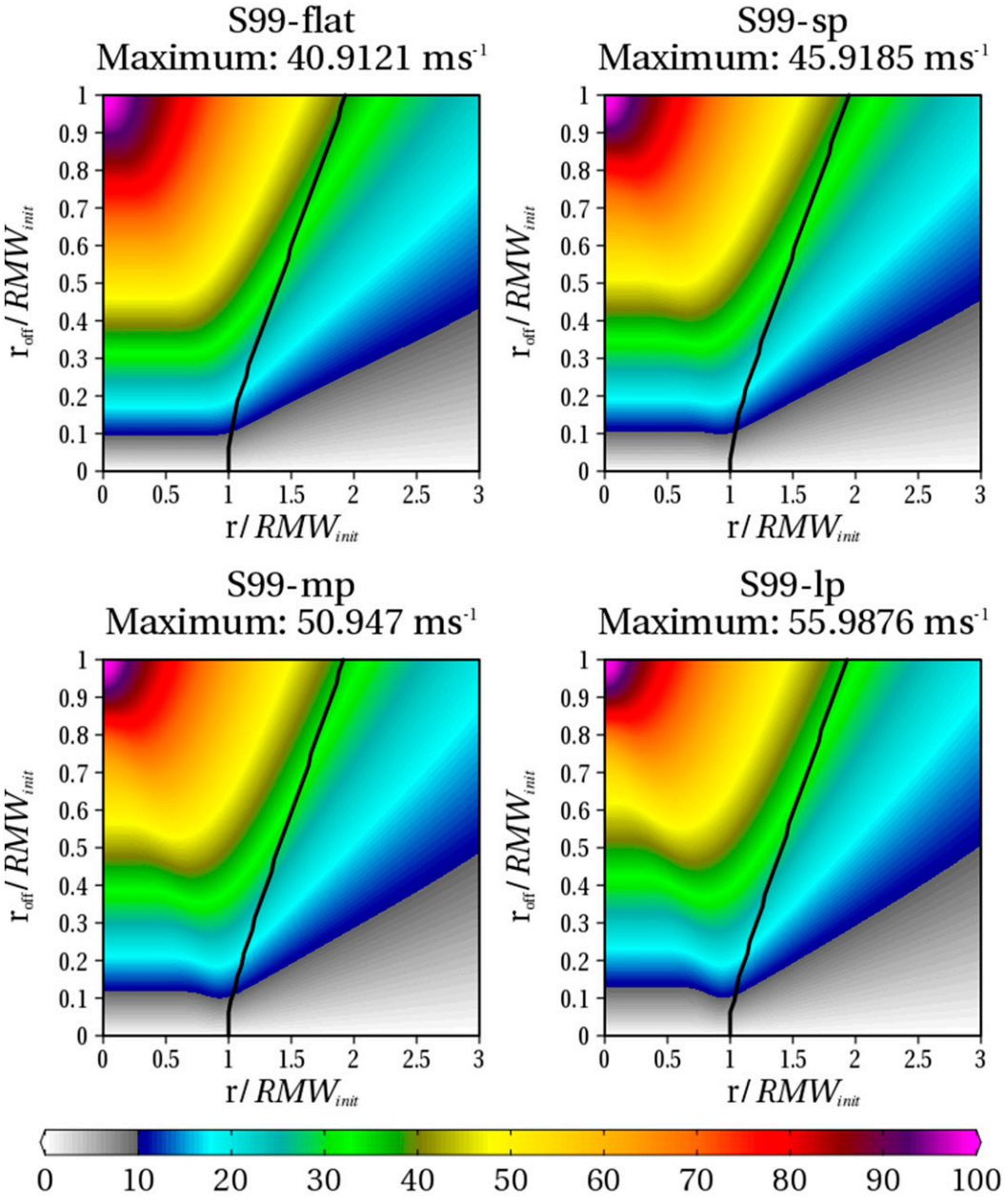

FIG. 13. As in Fig. 12, but for wavenumber 1 radial wind field.

asymmetry, then the RMW increases in size even faster than in the original profile. The MMTW error profile, however, barely changes among the four profiles.

The error profiles of vorticity for the three vortices are shown in Fig. 21. The general symmetric and wavenumber 1 structures are very similar in all three, indicating that once again, the primary factor controlling these error profiles is the symmetric tangential profile. When the center is moved in the direction of the largest anomaly (Guillermo-final), then the maximum values of vorticity are no longer located just inside the original RMW. Wavenumber 1 error profiles look very similar to the ones shown in previous sections. Where the differences start to appear more prominently is in wavenumber 2 and beyond. While the general shape of the error profiles are similar such that it is evident that the symmetric profile is the main source of error, the nuanced differences among the three profiles become quite prominent. To demonstrate how this may affect diagnostic analysis, Fig. 22 is a comparison of Fourier amplitudes at the RMW for the four Guillermo-based profiles. Wavenumber 2, the wavenumber that could be

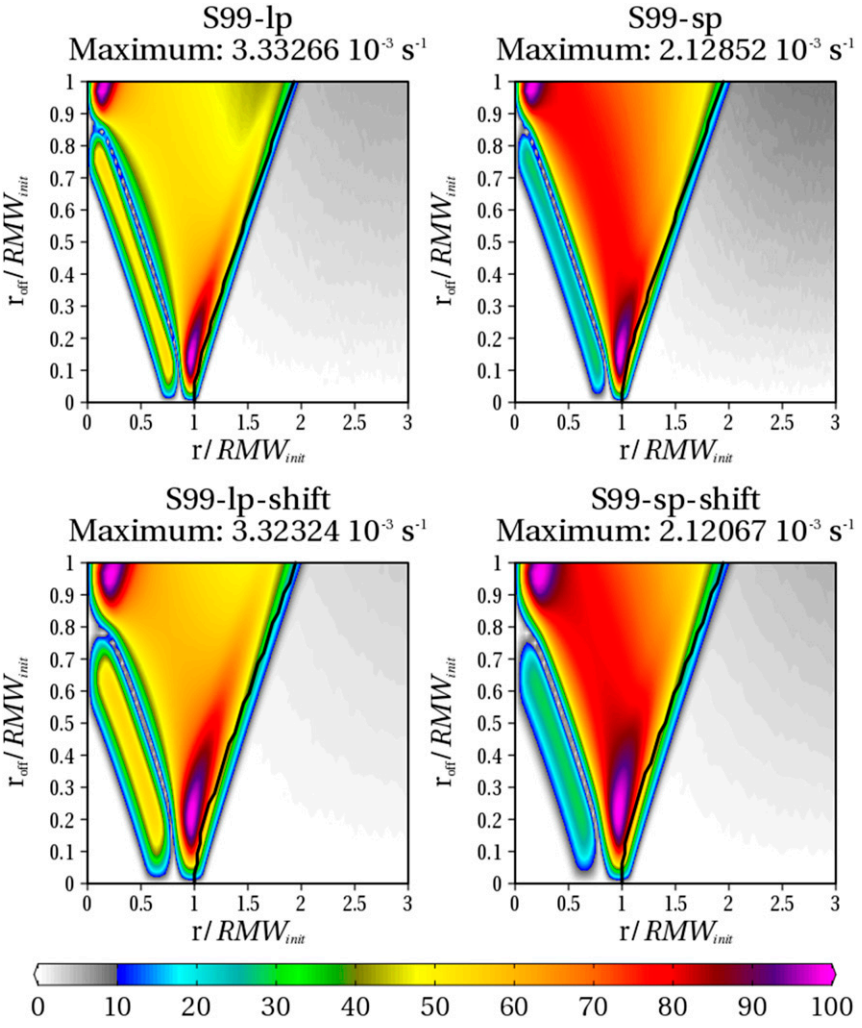

FIG. 14. As in Fig. 12, but for S99-lp, S99-sp, large peak shifted inward (S99-lp-shift), and small peak shifted inward (S99-sp-shift).

useful for determining whether a vortex is elliptical, behaves slightly erratically at low offsets, both increasing and decreasing here in a narrow offset band. This would indicate that caution may be needed when assessing ellipticity of a vortex.

Figure 23 shows the differences between Guillermo-final and Guillermo-final-rot for the Fourier amplitudes of vorticity, tangential wind, and radial wind. Evidently, beyond just the symmetric profiles seen before, there exists much variability when multiple asymmetries are introduced. For vorticity, when moving toward the vorticity maximum, there exists a small increase in the mean profile at the RMW and also a secondary maximum toward inner radii, peaking at the instance where the center is located directly inside the large asymmetry (0.9 offset). This movement also results in a larger response in all vorticity wavenumbers shown here when compared with a rotated asymmetry. The difference structures, however, become far more chaotic at higher wavenumbers, as aliasing errors spread out across other wavenumbers. For tangential wind, the asymmetries are generally much smaller than the symmetric profile. These values are between 1 and 5 m s^{-1}, whereas the peak MMTW is 55 m s^{-1}. Radial wind structures are also much smaller than their respective symmetric-error counterparts. This indicates that postprocessing information based on one center can be very difficult and inconsistent when asymmetries are present, especially vorticity-based analyses.

5. Summary and discussion

In this paper, we have attempted to break down and explore more thoroughly possible errors associated with

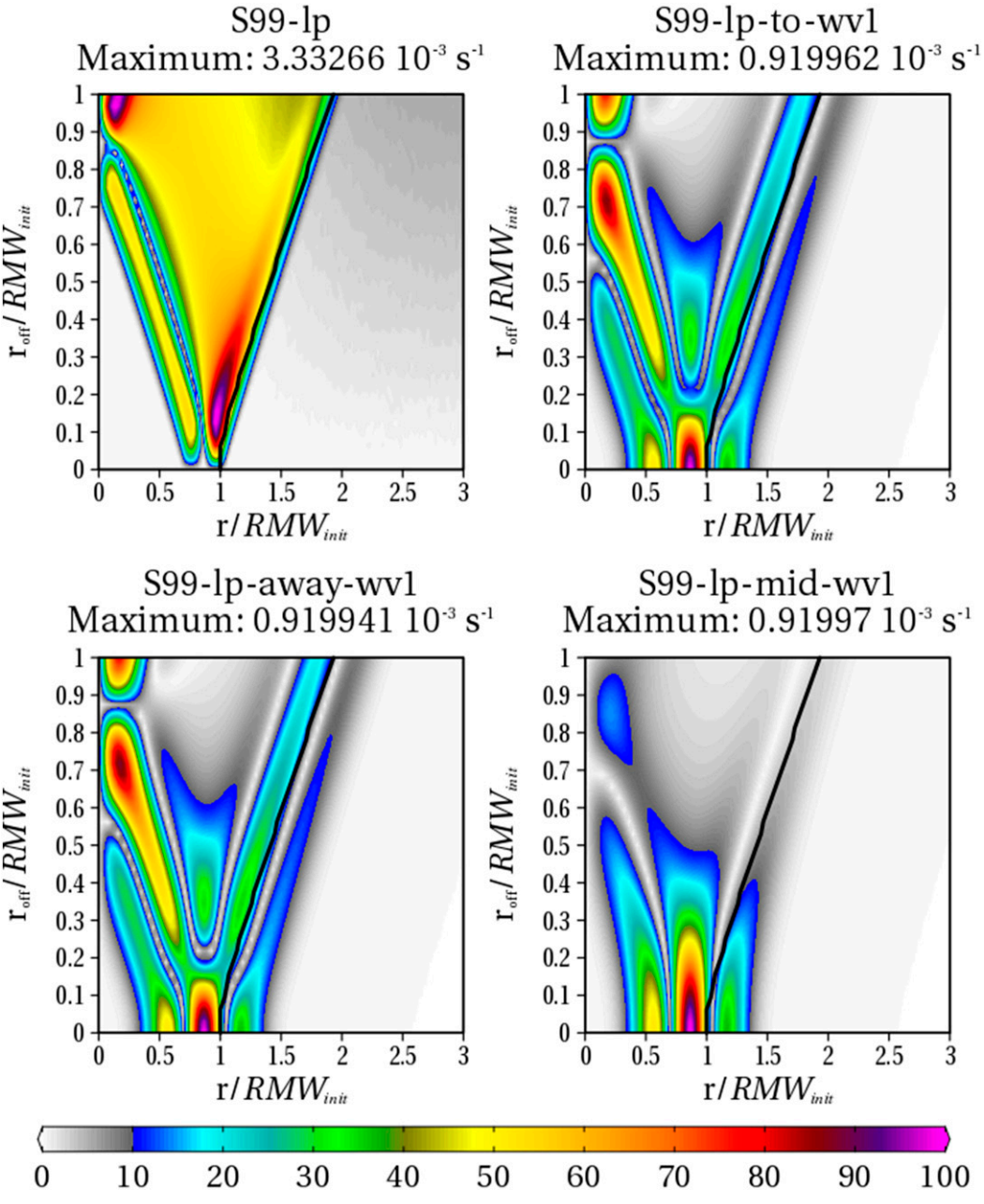

FIG. 15. As in Fig. 12, but for S99-lp and three Gaussian wavenumber 1 perturbations (no symmetric field). The offset vector is toward the maximum (to-wv1), toward the minimum (away-wv1), or where the perturbation is zero (mid-wv1).

center placement of mature tropical cyclones. We presented an expanded analysis of RH15's dataset—2012 TCs North Atlantic Debby, east Pacific Danny, and east Pacific Emilia simulated in HWRF, COTC, and GFDL, respectively—which included a relative spread calculation and a Fourier analysis of Hurricane Emilia from 2012 in HWRF. We showed that, despite the fact that absolute spread, defined as root-mean-square distance from a mean of the centers, appears to depend on intensity, relative spread (the unitless spread divided by the RMW) does not show a strong relationship with intensity. Over the RH15 dataset, the median relative spread value is approximately 0.225. Through azimuthal Fourier analyses, we showed that most of the differences occur in potential vorticity and radial wind. We also showed that the MMTW is less sensitive to a changing

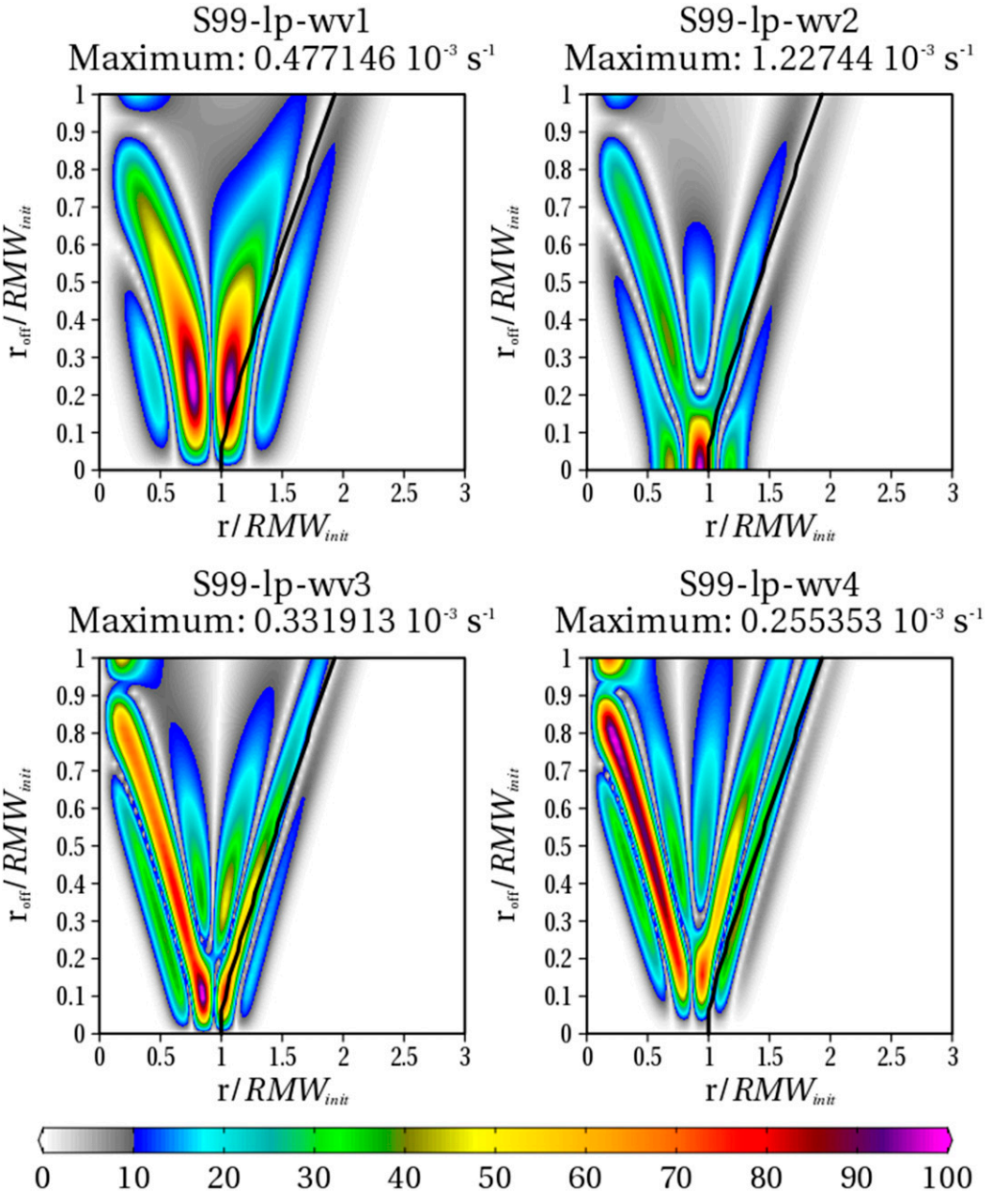

FIG. 16. Normalized wavenumber 2 error profiles for isolated asymmetries. Each asymmetry is placed on the S99-lp vortex and then analyzed in isolation, with the offset being moved along the zero axis. The magnitudes of the original vorticity asymmetries are 0.914, 1.23, 0.740, and 0.665 (10^{-3} s^{-1}) for each respective asymmetry.

center than the RMW. It is difficult to postulate meaningful analyses of these profiles, however, because of the inherent complexity of the simulations in HWRF and the lack of a "true" center. To compensate for this, we chose to build idealized vortices using two peer-reviewed parametric vortex construction methods: a wind-based one from WDR and a vorticity-based one from S99. We converted these profiles to streamfunctions and then added Gaussian perturbations. This is done in order to maintain physical consistency between vorticity and wind fields. If necessary, a symmetric radial wind field with a lognormal-in-radius profile was added followed by a background wind field. Multiple profiles using both the WDR and the S99 methods were analyzed.

The first profile analyzed using the WDR method is from the source reference, Hurricane Diana from 1984, and is tangential wind only. The center used for

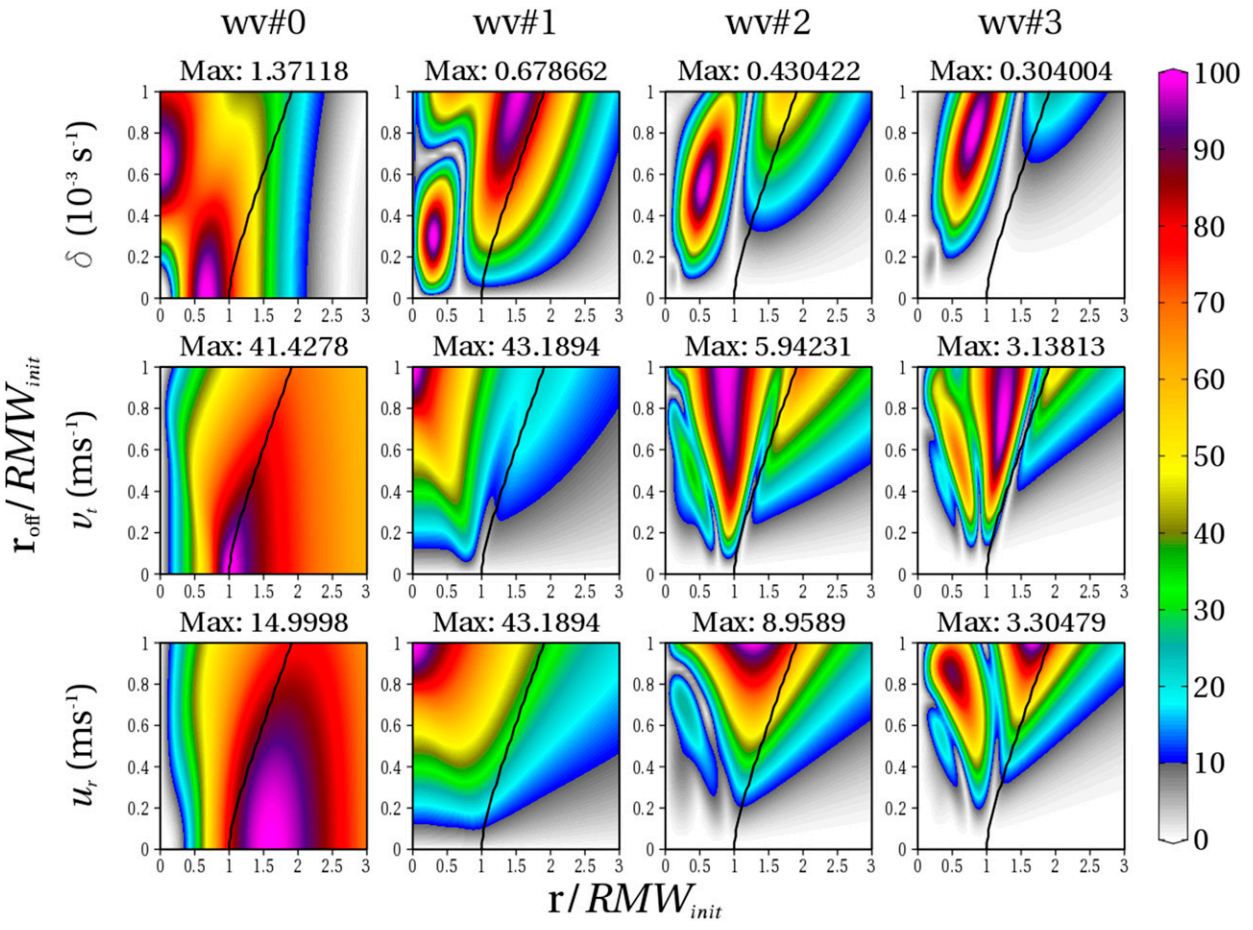

FIG. 17. Error profiles of normalized azimuthal Fourier amplitudes of divergence, tangential wind, and radial wind for the WDR Diana profile with symmetric radial inflow.

calculations—which, when normalized by the RMW distance, is defined as an offset—was displaced from the true center to the RMW in 32 increments. At each offset, Fourier analyses were performed to demonstrate aliasing errors. It was shown that the tangential wind aliasing errors are located primarily inside the RMW, while primarily wavenumber 1 radial wind asymmetries stretch over the breadth of the storm. Trigonometric expressions were derived to explain why radial wind is more sensitive than tangential wind. Vorticity asymmetries peak at offsets of 0.2, 0.3, and 0.35 for wavenumbers 1, 2, and 3, respectively. The values here appear to be nonnegligible when compared with the mean, on the order of the mean values itself. These offsets are relevant given the information presented on the spread/RMW analyses of the RH15 dataset.

Using various symmetric vortices from the S99 method, it was shown that RMW and MMTW error profiles do not vary significantly based on inner-core vortex profile. In fact, the change of the MMTW with respect to the offset is smallest, and only slightly, when the difference between the peak wind and the wind at outer radii is small. The projection of symmetric vorticity to higher wavenumbers is dependent on both size of the core and the difference between the peak vorticity and the inner-core vorticity. Smaller storms show larger areas of aliased error, while storms with higher peak vorticity values have more localized areas of larger errors.

Adding additional components to the vortex unsurprisingly complicates the error profiles. The aliasing error structures of asymmetries, for example, depend not only on the intensity of the asymmetries but also on the location of the asymmetries relative to the center. When adding a symmetric radial wind component, the primary aliasing error is manifested in both the divergence field and the wavenumber 1 tangential wind field, albeit weakly in the latter case. A straight-line background wind field adds to the wavenumber 1 components of the flow. Finally, when multiple asymmetries

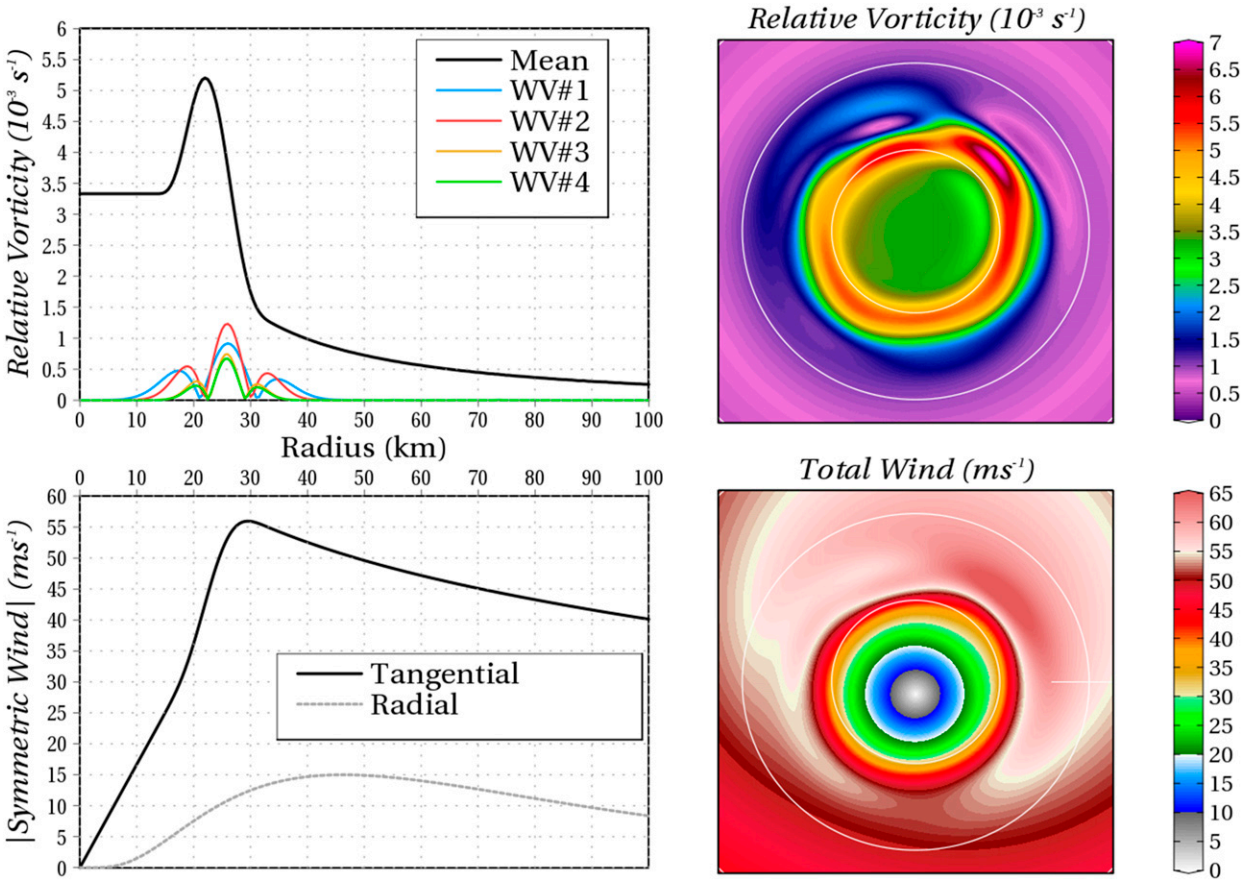

FIG. 18. Initial conditions for the Guillermo-like vortex. Fourier amplitudes are absolute values. White rings are 20-km radial contours. For this vortex, all center offsets are moved to the northeast from the starting position to the RMW.

with different phases are added, there exists the potential for noticeable change in RMW calculation depending on how a center is positioned relative to a large asymmetry.

The underlying theme consistent throughout section 4 is that the aliasing error of the symmetric mode is the dominant signal in error profiles, while asymmetric structures add nuance. Given the plethora of center-finding methods, we propose two solutions to the question of "Which center do I choose?" First, given the example of Emilia in HWRF and the results presented here, the best possible solution is to use multiple centers to test the robustness of physical features on and around the eyewall. Perhaps some sort of statistical post-processing could further clarify the physicality of the results in a probabilistic way. Second, if one were to choose one and only one method for determining the center in order to compute dynamical quantities in cylindrical coordinates such as azimuthal Fourier components or eddy-mean flux calculations, then we would suggest using a technique that seeks to maximize the mean. From RH15, that would be the MAVWBS method—the method that iterates over a fixed number of grid points to find the RMW and then uses the HRD's simplex method to fine-tune those results. The reason we suggest this is that from the analyses presented here, the error of the mean can only be aliased to higher wavenumbers in a consistent and somewhat predictable way, whereas errors from asymmetries are very dependent on the relative location of those asymmetries with respect to the calculated center. Additionally, the upscale aliasing is small given a reasonably calculated center. One has to make a choice on which information needs to be preserved and which needs to be sacrificed. Given this dilemma, we would suggest preserving the mean and sacrificing some of the higher-order asymmetric information. Using this as a mindset, we would argue for the HWRF Emilia example at 850 hPa, the RMW is 36 km, the MMTW is 61 m s^{-1}, and the wavenumber 1 PV value of approximately 1 PVU peaked at 26 km most closely represents the physical reality. For similar reasons, we would also state that, for example,

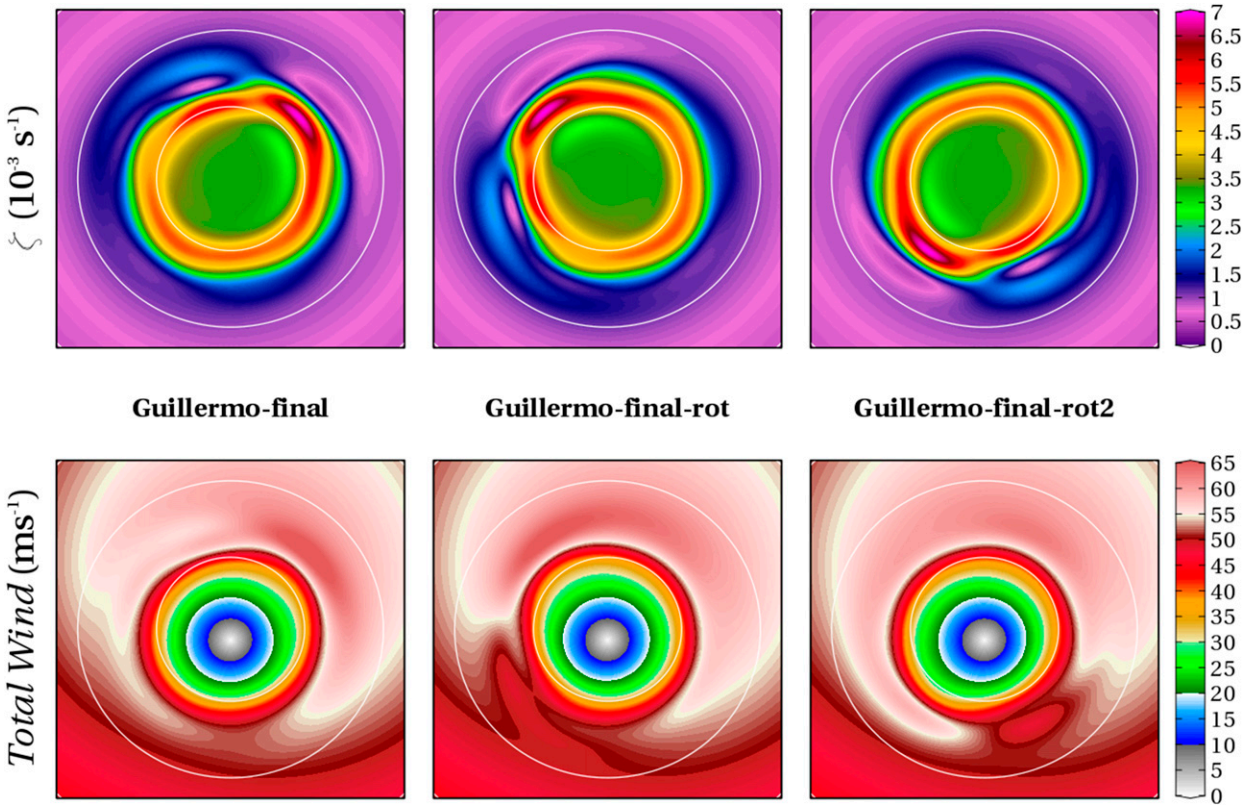

FIG. 19. The three Guillermo-based profiles. In each profile, the center is displaced to the northeast, stopping at the RMW.

the wavenumber 2 prominence shown by Reasor et al. (2009) is also a physical reality with minimal computational error. Both use HRD's simplex method to find the center.

An important distinction we would like to make is the difference between physical realities and computational artifacts. When a tropical cyclone evolves, whether in a model or in nature, it does so according to whatever physical processes are dominant at the time in shaping its evolution—processes such as environmental flow, boundary layer turbulence, barotropic eyewall breakdown, sea surface fluxes, convective processes, and so on. These physical processes occur regardless of the viewer's perspective. Where the ambiguity lies is in determining the components of these for storm-relative postprocessing analyses. For example, in Fig. 9, at an offset of 0.1, there is a wavenumber 1 radial flow of approximately 4 m s^{-1} at the RMW. That radial flow is obviously nonphysical, as the vortex is prescribed as tangential flow only, and is a computational artifact; however, the magnitude of the total wind of the vortex does not change, only our storm-relative perspective of the components of that wind changes. Optimally, what one would do is use multiple centers to test the physical robustness of a feature, as seen in Emilia in section 2. Several centers indicate a PV wavenumber 1 of 1 PVU, which agrees with the MAVWBS solution.

An important caveat here is that we suggest the MAVWBS method and those of its ilk (e.g., Xu et al. 2015) for *two-dimensional* dynamical analyses; this is most certainly *not* the suggestion for 3D analyses. Observations sometimes indicate dynamically coevolving centers (Black et al. 1972), and we feel that it is useful not only to discuss the location of centers in isolation based on a certain dynamic parameter (circulation maximum, pressure minimum, PV centroid, etc.) but also to discuss how those centers evolve with respect to each other. That discussion is reserved for Part II of this series. Additionally, this work neglects the beginning and end times of a TC's life cycle—genesis and extratropical transition (if applicable), respectively. These are both important topics that need investigation, as the reasoning behind using the MAV methods—wavenumber 0 is the dominant mode—begins to falter.

Last, we would like to suggest that the results of this manuscript extend beyond the direct or diagnostic analysis of TC structure. We speculate that our results have important ramifications to the assimilation of

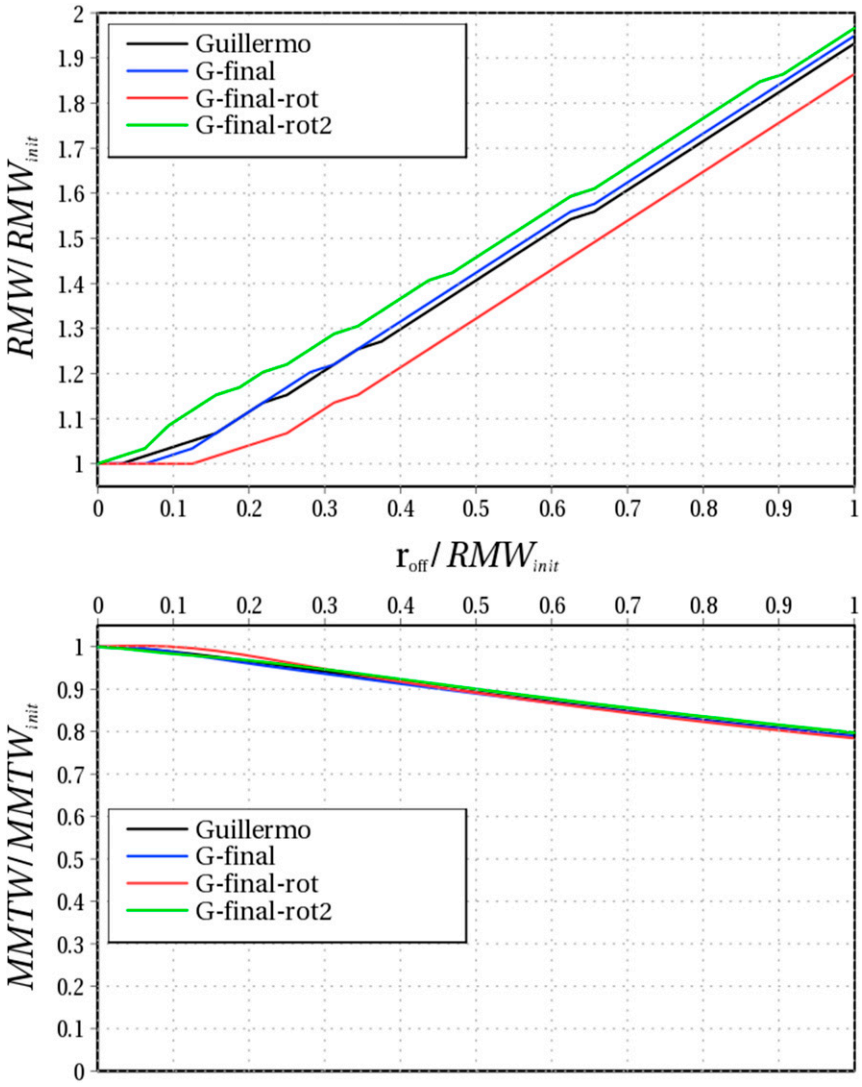

FIG. 20. As in Fig. 11, but for the Guillermo-based profiles. Guillermo (black line) is only the symmetric component of the tangential winds.

observations of tropical cyclone parameters in ensemble data assimilation algorithms. Previous work in ensemble data assimilation has assimilated observations of tropical cyclone center and various measures of intensity (e.g., Wu et al. 2010; Chen and Snyder 2007). For example, Wu et al. (2010) assimilated TC position by identifying the TC center using a geopotential anomaly centroid method with a 300-km box averaging region in their ensemble Kalman filter algorithm. RH15 has shown that the use of a large box in a centroid method (where 300 km is considered to be large relative to the size of the RMW) is likely to lead to a larger sensitivity to the outer portions of the storm when the inner-core vortex is potentially of more interest. In an ensemble method this center finding must be done to each member, and this additional noise in each member can result in a degradation of the state estimate at the end of the assimilation and/or a substantially larger observation error variance than what would be required with an accurate center-finding algorithm. Similarly, the act of finding the center of each ensemble member must technically be done consistently with the way the center of the TC is found for the observation. If the observation of TC center is accurate and unbiased, then so must be the result of the method to identify the center of each ensemble member. Last, Wu et al. (2010) also assimilated observations of TC intensity based on a fit to the WDR profile of various observational data. Our results suggest that because their geopotential centroid method provides a TC center that does not necessarily favor the

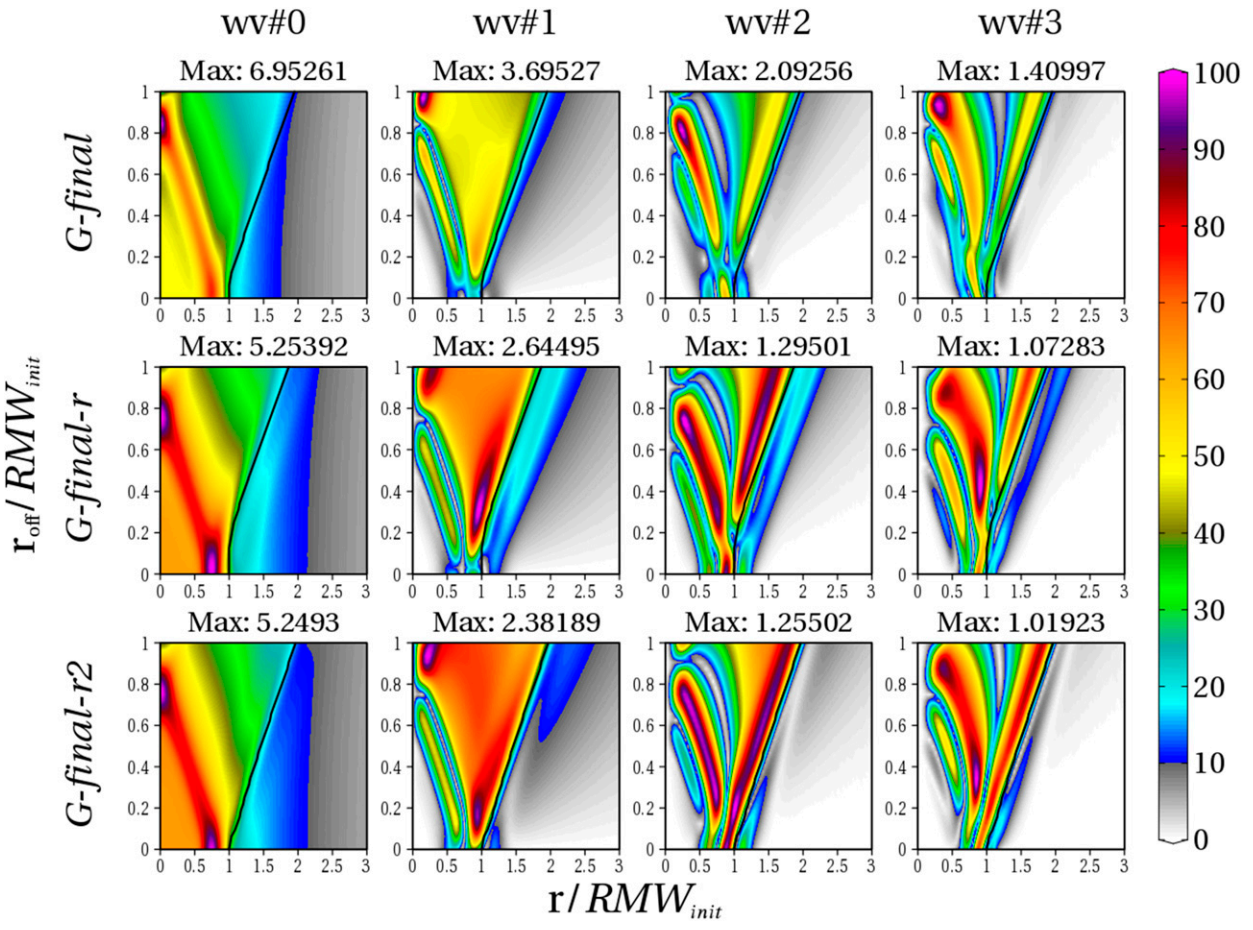

FIG. 21. Error profiles of the normalized azimuthal Fourier amplitudes of vorticity (10^{-3} s^{-1}) for the three Guillermo profiles with asymmetries.

RMW, they systematically underestimated the resulting storm fit to the WDR profile, in a similar way as to what was seen in our Figs. 8 and 11. The impact of this was a weakening of the relationship between the intensity and the state space to be updated by the algorithm, which implies, in the end, an analyzed storm that is less consistent with the observations. All of these results suggest caution, and a careful comparison of the impact of different center-finding methods on ensemble data assimilation is required. Ultimately, it is worth investigating how sensitive model simulations are to the structure of the initialized vortex. Work in this direction is under way.

Acknowledgments. A portion of this work was performed while author DRR was employed at Fleet Numerical Meteorology and Oceanography Center, Monterey, CA. He is currently supported by a National Research Council Postdoctoral Research Award at the Naval Research Laboratory Marine Meteorology Division. Author Hodyss gratefully acknowledges support from the Office of Naval Research PE-0601153N. We thank Robert Hart and James Doyle for their contributions to this work and three anonymous reviewers whose insightful comments helped to improve this work's clarity and content.

APPENDIX A

Derivation of Lognormal Wind Profile

The derivation of Eq. (5) begins by declaring what we desire, which is a radial wind profile that is lognormal in radius but has a prescribed maximum value and location:

$$\overline{U}(r) = U_{\max}\frac{f_X(r)}{f_X(r_0)}, \tag{A1}$$

where f_X is the lognormal function (Wilks 2011, 91–92):

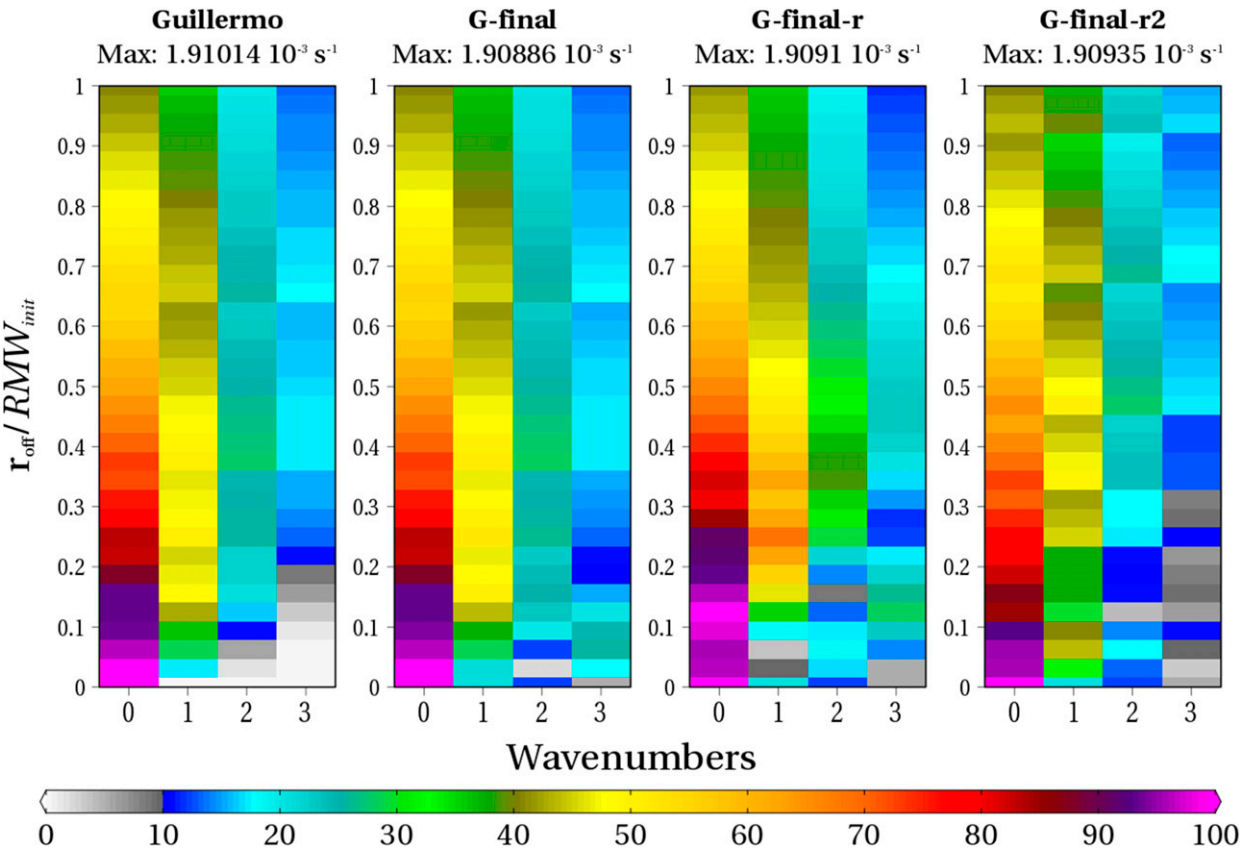

FIG. 22. Normalized Fourier amplitudes of vorticity at the RMW of that particular offset for the four Guillermo profiles.

$$f_X(r) = \frac{1}{t\sqrt{2\pi}}\frac{1}{r}\exp\left[-\frac{(\ln r - s)^2}{2t^2}\right]; \qquad \text{(A2)}$$

r_0 is the radius of maximum radial winds (RMRW) and s and t are constants describing the distribution and are always greater than zero. The variable S is the location parameter and t is the shape parameter. The RMRW is the analog of the mode of a lognormal distribution, which can be expressed as

$$\text{RMRW} \equiv r_0 = e^{s-t^2}, \qquad \text{(A3)}$$

where s is always larger than r_0. This can be substituted into Eq. (A2) to yield

$$f_X(r_0) = \frac{1}{t\sqrt{2\pi}}\exp\left(-s + \frac{t^2}{2}\right). \qquad \text{(A4)}$$

Equation (A4) can be substituted into Eq. (A1), resulting in the lognormal wind profile:

$$\overline{U}(r) = \frac{U_{\max}}{r}\exp\left\{s - \frac{t^2}{2} - \left[\frac{(\ln r - s)^2}{2t^2}\right]\right\}. \qquad \text{(A5)}$$

For this particular work, we have chosen to prescribe the location parameter s, where s is the natural logarithm of a "mean" radius, and then to solve for the shape parameter t. Setting r equal to r_0, setting the wind speed to $U_{\max}$, and performing the requisite algebra yields a quartic equation in t:

$$\frac{1}{2}t^4 + (s - \ln r_0)t^2 - \frac{(\ln r_0 - s)^2}{2} = 0. \qquad \text{(A6)}$$

This equation is then solved computationally using Newton's method for t, and the positive (double) root is chosen. Combined, these two give the shape of the distribution. If s is very close to $\ln r_0$, then the shape of the wind field will be steeper. If s is farther away, then the wind field will be much more diffuse.

APPENDIX B

Derivation of Relationship between Aliased Winds

Determining the center of a tropical cyclone is what controls the ambiguity of how a wind vector at a given point is decomposed into its cylindrical components. In a

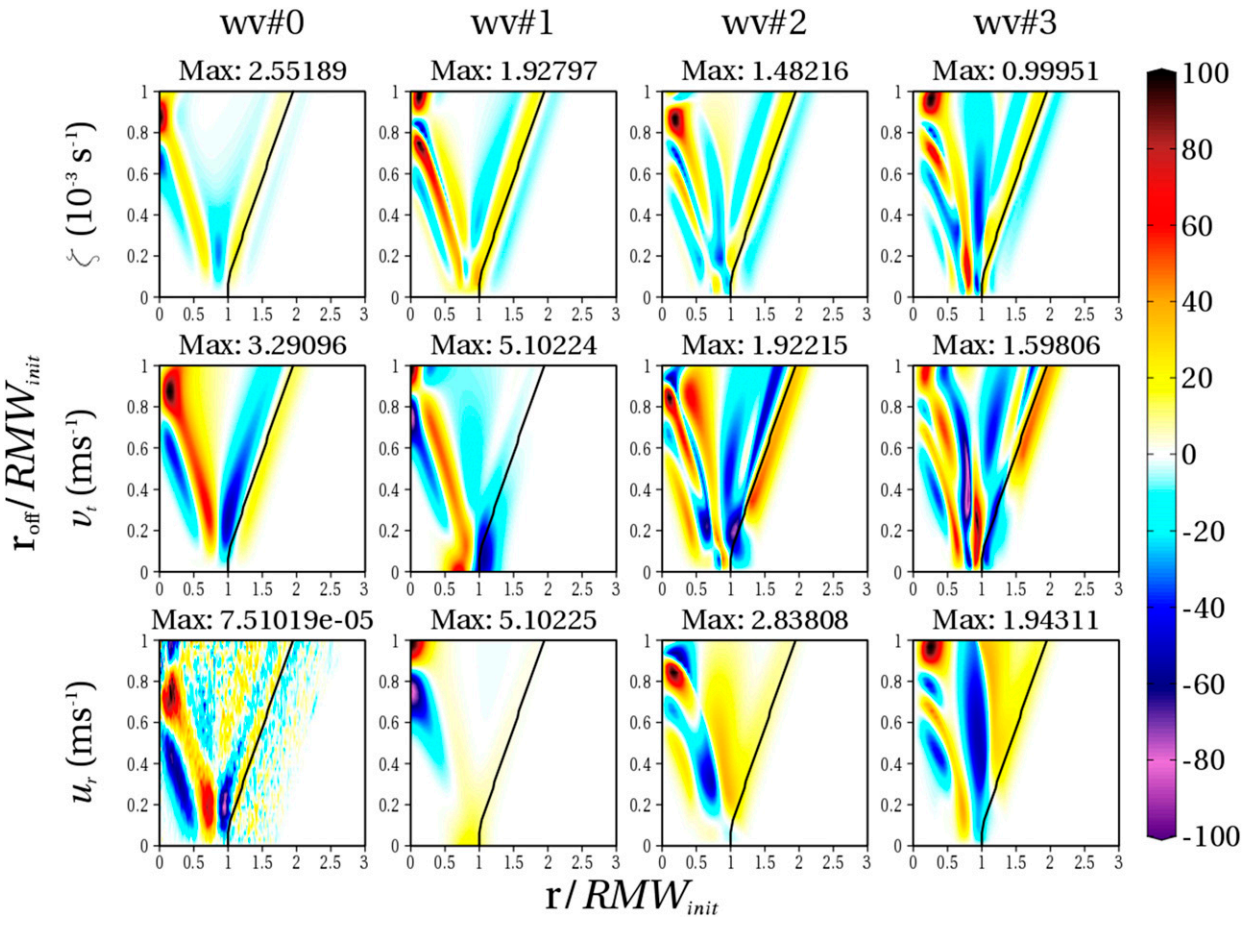

FIG. 23. Normalized azimuthal Fourier differences of vorticity, tangential wind, and radial wind between Guillermo-final and Guillermo-final-rot. Warm (cool) colors indicate values where Guillermo-final (Guillermo-final-rot) is larger.

fixed, Earth-relative (i.e., Cartesian) frame of reference at a given moment in time, the Cartesian wind components remain fixed. The storm-relative cylindrical wind components, however, change depending on the location of the center and, thus, the perspective of the observer. To explain the sensitivity, we start with the four conversion equations for the wind components in cylindrical and Cartesian coordinates:

$$v_t = v_y \cos\theta - u_x \sin\theta, \tag{B1a}$$

$$u_r = u_x \cos\theta + v_y \sin\theta, \tag{B1b}$$

$$v_y = v_t \cos\theta + u_r \sin\theta, \quad \text{and} \tag{B1c}$$

$$u_x = u_r \cos\theta - v_t \sin\theta, \tag{B1d}$$

where the subscripts indicate the coordinate system: x and y for Cartesian, r and t for cylindrical. The variable θ is the angle between a grid point and a center location. Imagine we have two centers on a vortex defined by o and n, where o is the original center and n is some new center at an offset. Taking advantage of the fact that the Cartesian wind components are fixed in space, we can express tangential and radial winds relative to the new center n in terms of tangential and radial winds relative to the old center o:

$$\begin{aligned} v_t^n = {} & (v_t^o \cos\theta_o + u_r^o \sin\theta_o)\cos\theta_n \\ & - (u_r^o \cos\theta_o - v_t^o \sin\theta_o)\sin\theta_n \quad \text{and} \end{aligned} \tag{B2a}$$

$$\begin{aligned} u_r^n = {} & (u_r^o \cos\theta_o - v_t^o \sin\theta_o)\cos\theta_n \\ & + (v_t^o \cos\theta_o + u_r^o \sin\theta_o)\sin\theta_n. \end{aligned} \tag{B2b}$$

To simplify, we will assume the vortex is as WDR Diana in section 4a, where the winds are only tangential around the true center, o. Simplifying and using a trigonometric identity yield

$$\begin{aligned} v_t^n &= v_t^o \cos\theta_o \cos\theta_n + v_t^o \sin\theta_o \sin\theta_n \\ &= v_t^o \cos(\theta_n - \theta_o) \quad \text{and} \end{aligned} \tag{B3a}$$

$$\begin{aligned} u_r^n &= -v_t^o \sin\theta_o \cos\theta_n + v_t^o \cos\theta_o \sin\theta_n \\ &= v_t^o \sin(\theta_n - \theta_o). \end{aligned} \tag{B3b}$$

Since the sine function is more sensitive to small changes in angle at small angles, radial wind aliasing from the tangential wind is more sensitive over the entirety of the storm. The tangential wind is more robust until angle differences become larger, something that would happen closer to the moved center—generally, inside the RMW. For example, with a 10° difference, the tangential wind would still retain 98.5% of its initial value, while the radial wind would gain 17.4% of the value of the initial tangential wind. Note that total wind magnitude is what is conserved:

$$\begin{aligned}\|\mathbf{v}\| &= \sqrt{(u_x)^2 + (v_y)^2} = \sqrt{(u_r^n)^2 + (v_t^n)^2} \\ &= \sqrt{(v_t^o)^2 \cos^2(\theta_n - \theta_0) + (v_t^o)^2 \sin^2(\theta_n - \theta_o)} \\ &= |v_t^o|. \end{aligned} \tag{B4}$$

REFERENCES

Bender, M. A., I. Ginis, R. Tuleya, B. Thomas, and T. Marchok, 2007: The operational GFDL coupled hurricane–ocean prediction system and a summary of its performance. *Mon. Wea. Rev.*, **135**, 3965–3989, doi:10.1175/2007MWR2032.1.

Black, P. G., H. V. Senn, and C. L. Courtright, 1972: Airborne observations of eye configuration changes, bright band distribution, and precipitation tilt during the 1969 multiple seeding experiments in Hurricane Debby. *Mon. Wea. Rev.*, **100**, 208–217, doi:10.1175/1520-0493(1972)100<0208:AROOEC>2.3.CO;2.

Braun, S. A., and L. Wu, 2007: A numerical study of Hurricane Erin (2001). Part II: Shear and the organization of eyewall vertical motion. *Mon. Wea. Rev.*, **135**, 1179–1194, doi:10.1175/MWR3336.1.

Chen, Y., and C. Snyder, 2007: Assimilating vortex position with an ensemble Kalman filter. *Mon. Wea. Rev.*, **135**, 1828–1845, doi:10.1175/MWR3351.1.

Cram, T. A., J. Persing, M. T. Montgomery, and S. A. Braun, 2007: A Lagrangian trajectory view on transport and mixing processes between the eye, eyewall, and environment using a high-resolution simulation of Hurricane Bonnie (1998). *J. Atmos. Sci.*, **64**, 1835–1856, doi:10.1175/JAS3921.1.

Davis, C., S. C. Jones, and M. Riemer, 2008: Hurricane vortex dynamics during Atlantic extratropical transition. *J. Atmos. Sci.*, **65**, 714–736, doi:10.1175/2007JAS2488.1.

Doyle, J. D., and Coauthors, 2012: Real-time tropical cyclone prediction using COAMPS-TC. *Advances in Geophysics*, Vol. 28, Academic Press, 15–28, doi:10.1142/9789814405683_0002.

Frank, W. M., and E. A. Ritchie, 1999: Effects of environmental flow upon tropical cyclone structure. *Mon. Wea. Rev.*, **127**, 2044–2061, doi:10.1175/1520-0493(1999)127<2044:EOEFUT>2.0.CO;2.

——, and ——, 2001: Effects of vertical wind shear on the intensity and structure of numerically simulated hurricanes. *Mon. Wea. Rev.*, **129**, 2249–2269, doi:10.1175/1520-0493(2001)129<2249:EOVWSO>2.0.CO;2.

Gopalakrishnan, S. G., S. Goldberg, T. Quirino, X. Zhang, F. Marks, K.-S. Yeh, R. Atlas, and V. Tallapragada, 2012: Toward improving high-resolution numerical hurricane forecasting:Influence of model horizontal grid resolution, initialization, and physics. *Wea. Forecasting*, **27**, 647–666, doi:10.1175/WAF-D-11-00055.1.

Hart, R. E., 2003: A cyclone phase space derived from thermal wind and thermal asymmetry. *Mon. Wea. Rev.*, **131**, 585–616, doi:10.1175/1520-0493(2003)131<0585:ACPSDF>2.0.CO;2.

Hendricks, E. A., W. H. Schubert, R. K. Taft, H. Wang, and J. P. Kossin, 2009: Life cycles of hurricane-like vorticity rings. *J. Atmos. Sci.*, **66**, 705–722, doi:10.1175/2008JAS2820.1.

——, B. D. McNoldy, and W. H. Schubert, 2012: Observed inner-core structural variability in Hurricane Dolly (2008). *Mon. Wea. Rev.*, **140**, 4066–4077, doi:10.1175/MWR-D-12-00018.1.

Jones, S. C., 1995: The evolution of vortices in vertical shear. Part I: Initially barotropic vortices. *Quart. J. Roy. Meteor. Soc.*, **121**, 821–851, doi:10.1002/qj.49712152406.

Kepert, J. D., 2006: Observed boundary layer wind structure and balance in the hurricane core. Part I: Hurricane Georges. *J. Atmos. Sci.*, **63**, 2169–2193, doi:10.1175/JAS3745.1.

Kwon, Y. K., and W. M. Frank, 2005: Dynamic instabilities of simulated hurricane-like vortices and their impacts on core structure of hurricanes. Part I: Dry experiments. *J. Atmos. Sci.*, **62**, 3955–3973, doi:10.1175/JAS3575.1.

——, and ——, 2008: Dynamic instabilities of simulated hurricane-like vortices and their impacts on core structure of hurricanes. Part II: Moist experiments. *J. Atmos. Sci.*, **65**, 106–122, doi:10.1175/2007JAS2132.1.

Mallen, K. J., M. T. Montgomery, and B. Wang, 2005: Re-examining the near-core radial structure of the tropical cyclone primary circulation: Implications for vortex resiliency. *J. Atmos. Sci.*, **62**, 408–425, doi:10.1175/JAS-3377.1.

Marchok, T. P., 2002: How the NCEP tropical cyclone tracker works. Preprints, *25th Conf. on Hurricanes and Tropical Meteorology*, San Diego, CA, Amer. Meteor. Soc., P1.13. [Available online at https://ams.confex.com/ams/25HURR/techprogram/paper_37628.htm.]

Marks, F. D., R. A. Houze, and J. F. Gamache, 1992: Dual-aircraft investigation of the inner core of Hurricane Norbert. Part I: Kinematic structure. *J. Atmos. Sci.*, **49**, 919–942, doi:10.1175/1520-0469(1992)049<0919:DAIOTI>2.0.CO;2.

Montgomery, M. T., J. Zhang, and R. K. Smith, 2014: An analysis of the observed low-level structure of rapidly intensifying Hurricane Earl (2010). *Quart. J. Roy. Meteor. Soc.*, **140**, 2132–2146, doi:10.1002/qj.2283.

Nguyen, L. T., J. Molinari, and D. Thomas, 2014: Evaluation of tropical cyclone identification methods in numerical models. *Mon. Wea. Rev.*, **142**, 4326–4339, doi:10.1175/MWR-D-14-00044.1.

Powell, M. D., and T. A. Reinhold, 2007: Tropical cyclone destructive potential by integrated kinetic energy. *Bull. Amer. Meteor. Soc.*, **88**, 513–526, doi:10.1175/BAMS-88-4-513.

Reasor, P. D., and M. T. Montgomery, 2001: Three-dimensional alignment and corotation of weak, TC-like vortices via linear vortex Rossby waves. *J. Atmos. Sci.*, **58**, 2306–2330, doi:10.1175/1520-0469(2001)058<2306:TDAACO>2.0.CO;2.

——, and M. D. Eastin, 2012: Rapidly intensifying Hurricane Guillermo (1997). Part II: Resilience in shear. *Mon. Wea. Rev.*, **140**, 425–444, doi:10.1175/MWR-D-11-00080.1.

——, ——, and J. F. Gamache, 2009: Rapidly intensifying Hurricane Guillermo (1997). Part I: Low-wavenumber structure and evolution. *Mon. Wea. Rev.*, **137**, 603–631, doi:10.1175/2008MWR2487.1.

——, R. Rogers, and S. Lorsolo, 2013: Environmental flow impacts on tropical cyclone structure diagnosed from airborne Doppler

radar composites. *Mon. Wea. Rev.*, **141**, 2949–2969, doi:10.1175/MWR-D-12-00334.1.

Riemer, M., M. T. Montgomery, and M. E. Nicholls, 2010: A new paradigm for intensity modification of tropical cyclones: Thermodynamic impact of the vertical wind shear on the inflow layer. *Atmos. Chem. Phys.*, **10**, 3163–3188, doi:10.5194/acp-10-3163-2010.

Ryglicki, D. R., 2015: An analysis of a barotropically-unstable, high-Rossby number vortex in shear. *J. Atmos. Sci.*, **72**, 2152–2177, doi:10.1175/JAS-D-14-0180.1.

——, and R. E. Hart, 2015: An investigation of center-finding techniques for tropical cyclones in mesoscale models. *J. Appl. Meteor. Climatol.*, **54**, 825–846, doi:10.1175/JAMC-D-14-0106.1.

Schubert, W. H., M. T. Montgomery, R. K. Taft, T. A. Guinn, S. R. Fulton, J. P. Kossin, and J. P. Edwards, 1999: Polygonal eyewalls, asymmetric eye contraction, and PV mixing in hurricanes. *J. Atmos. Sci.*, **56**, 1197–1223, doi:10.1175/1520-0469(1999)056<1197:PEAECA>2.0.CO;2.

Stern, D. S., and F. Zhang, 2013: How does the eye warm? Part II: Sensitivity to vertical wind shear and trajectory analysis. *J. Atmos. Sci.*, **70**, 1849–1873, doi:10.1175/JAS-D-12-0258.1.

Walsh, K. J. E., M. Fiorino, C. W. Landsea, and K. L. McInnes, 2007: Objectively determined resolution-dependent threshold criteria for the detection of tropical cyclones in climate models and reanalyses. *J. Climate*, **20**, 2307–2314, doi:10.1175/JCLI4074.1.

Wang, Y., and G. J. Holland, 1996: The beta drift of baroclinic vortices. part i: adiabatic vortices. *J. Atmos. Sci.*, **53**, 411–427, doi:10.1175/1520-0469(1996)053<0411:TBDOBV>2.0.CO;2.

Wilks, D. S., 2011: *Statistical Methods in the Atmospheric Sciences*. 3rd ed., Academic Press, 676 pp.

Willoughby, H. E., 1992: Linear motion of a shallow-water barotropic vortex as an initial-value problem. *J. Atmos. Sci.*, **49**, 2015–2031, doi:10.1175/1520-0469(1992)049<2015:LMOASW>2.0.CO;2.

——, and M. B. Chelmow, 1982: Objective determination of hurricane tracks from aircraft observations. *Mon. Wea. Rev.*, **110**, 1298–1305, doi:10.1175/1520-0493(1982)110<1298:ODOHTF>2.0.CO;2.

——, R. W. R. Darling, and M. E. Rahn, 2006: Parametric representation of the primary hurricane vortex. Part II: A new family of sectionally continuous profiles. *Mon. Wea. Rev.*, **134**, 1102–1120, doi:10.1175/MWR3106.1.

Wimmers, A. J., and C. S. Velden, 2010: Objectively determining the rotational center of tropical cyclones in passive microwave satellite imagery. *J. Appl. Meteor. Climatol.*, **49**, 2013–2034, doi:10.1175/2010JAMC2490.1.

Wu, C. C., G. Y. Lien, J. H. Chen, and F. Zhang, 2010: Assimilation of tropical cylone track and structure based on the ensemble Kalman filter (EnKF). *J. Atmos. Sci.*, **67**, 3806–3822, doi:10.1175/2010JAS3444.1.

Xu, Q., L. Wei, Y. Jin, Q. Zhao, and J. Cao, 2015: A dynamically constrained method for determining the vortex centers of tropical cyclones predicted by high-resolution models. *J. Atmos. Sci.*, **72**, 88–103, doi:10.1175/JAS-D-14-0090.1.

Zhang, J. A., W. M. Drennan, P. G. Black, and J. R. French, 2009: Turbulence structure of the hurricane boundary layer between the outer rainbands. *J. Atmos. Sci.*, **66**, 2455–2467, doi:10.1175/2009JAS2954.1.